2017

Engineering an Alkane-Hydroxylating Bacterial Monooxygenase: A Tale of Two Chemistries

Arjun Nanda
Pomona College

Engineering an Alkane-Hydroxylating Bacterial Monooxygenase: A Tale of Two Chemistries

Arjun Scott Nanda

Faculty Advisor: Professor Matthew Sazinsky
Second Reader: Professor Rou-jia Sung

Thesis submitted in partial fulfillment of the requirements
for the degree of Bachelor of Arts in Molecular Biology

Department of Molecular Biology

Pomona College, Claremont, CA
May 2017

Table of Contents

List of Abbreviations

AMO	Alkene monooxygenase
BMM	Bacterial multicomponent monooxygenase
C2,3O	Catechol 2,3 dioxygenase
DTT	Dithiothreitol
FAD	Flavin adenine dinucleotide
FPLC	Fast Protein Liquid Chromatography
H_{ox}	Oxidized/resting state of the diiron center of BMMs
H_{peroxo}	A peroxodiiron(III) reaction cycle intermediate
H_{red}	Reduced state of the diiron center of BMMs
IPTG	Isopropyl β-D-1-thiogalactopyranoside
LPC	*Lactobacillus plantarum* manganese catalase
LB	Luria Broth
MMO	Methane monooxygenase
sMMO	Soluble Methane Monooxygenase
sMMOB	Regulatory component of sMMO
sMMOR	Oxidoreductase component of sMMO
sMMOH	Hydroxylase component of sMMO
NADH	Nicotinamide Adenine Dinucleotide
NRVS	Nuclear Resonance Vibrational Spectroscopy
PDB	Protein Data Bank
Peroxide	Compounds containing oxygen–oxygen the peroxide anion, generally referring to hydrogen peroxide
PH	Phenol hydroxylase
PMSF	Phenylmethylsulfonyl fluoride
P*	Peroxodiiron(III) intermediate formed after reaction with O_2 in the sMMO and ToMO catalytic cycles
Q	Diamond core bis-μ-oxo diiron (IV) intermediate specific to the sMMO catalytic cycle
SsoMO	Hyperthermophilic toluene monooxygenase
T4MO	Toluene 4-monooxygenase
TCC	*Thermus thermophilus* manganese catalase
TCE	Tetrachloroethylene
THMO	Tetrahydrofuran/propane monooxygenases
TMO	Four-component alkene/aromatic monooxygenases
ToMO	Toluene/*o*-xylene monooxygenase
ToMOC	Oxidoreductase component of ToMO
ToMOD	Regulatory component of ToMO
ToMOF	Rieske-type component of ToMO
ToMOH	Hydroxylase component of ToMO

List of Figures

List of Tables

I. Abstract

Toluene / o-xylene monooxyenase (ToMO) from *Pseudomonas sp.* OX1 is a multimeric carboxylate-bridged diiron enzyme that efficiently catalyzes the hydroxylation of aromatic hydrocarbons with high specificity. Though included in a larger group of conserved bacterial multicomponent monooxygenases (BMMs) studied as potential biocatalysts for industrial hydrocarbon chemistry, the substrate specificity and oxygenated intermediates of ToMO differ greatly from its well-characterized, alkane hydroxylating analog – soluble methane monooxygenase (sMMO) from *Methylococcus capsulatus* and *Methylosinus trichosporium* OB3B. Despite a shared global topology and near identical active sites, sMMO utilizes a bis-μ-oxo diiron (IV) intermediate to cleave inert C-H bonds in alkanes while ToMO fails to hydroxylate alkanes by only accessing a peroxodiiron (III) species capable of oxidizing arenes, alkenes, and haloalkanes. Two seemingly similar structures give rise to vastly different chemistries. This work seeks to determine a structural basis for this difference by mutational analysis of residues thought to conformationally constrain the diiron catalytic center in ToMO, with the goal of replicating the terminal alkane hydroxylating activity of sMMO. To this end, a library of potential alkane-hydroxylating mutants generated through site-specific mutagenesis of constraining residues was kinetically characterized, revealing a range of novel behaviors including significant reaction rate enhancements as well as catalase-like breakdown of hydrogen peroxide. The double mutant E111A / T201S was found to weakly decompose hydrogen peroxide nearly ~100 fold slower than bovine liver catalase, but resist to peroxide-mediated inactivation normally observed in wild-type enzyme. In combination with low-level computational modeling to quantify the bulk and local rigidity of both sMMOH and ToMOH, this observed interaction between peroxide and the diiron center of different catalase-active mutants is used to propose a potential mechanism. With further comparison to other BMMs we suggest engineering a closely related peroxide shunt pathway, found to be inactive in wild-type and mutant ToMO variants, may be a path towards achieving alkane hydroxylation in ToMO. Methods to facilitate generation of this pathway through further mutagenesis are discussed, and the implications of the appearance of new reactive H_{peroxo} intermediates in the ToMO catalytic cycle are considered towards the eventual goal of understanding how modifying the protein scaffold of BMOs can influence metal center reactivity and achieve a variety of specific and efficient hydrocarbon chemistries.

II. Introduction

A. Bacterial Multicomponent monooxygenases

Bacterial multicomponent monooxygenases (BMMs) are a family of nonheme metalloenzymes that carry out the highly specific and thermodynamically efficient hydroxylation of hydrocarbons, aromatics, and alkenes at carboxylate-bridged diiron centers.[1–3] Originally identified for their role in assisting methanotrophs adapt to carbon-rich environments, the oxidative action of BMMs has since been studied for their role in global carbon regulation cycles, as well as a potential source of biocatalysts for industrial synthesis and bioremediation of organic pollutants.[1,4–6] With a broad range of substrate specificities, BMMs have received sustained interest as potential targets for efforts in rational protein engineering seeking to leverage these unique chemistries for wider applications.[7–11] BMM-mediated hydroxylase chemistry has contributed towards the effective degradation of harmful compounds such as tetrachloroethylene (TCE), as well as inspired the synthesis of inorganic catalysts capable of doing similar chemistry outside the context of a biological scaffold.[3,5,12]

As binuclear metalloenzymes, BMMs are also members of the ferritin-like superfamily of nonheme redox-active metalloproteins, which display a wide degree of activities beyond hydroxylation including iron storage in ferritin, O_2 transport in hemerythrin, radical formation in class II ribonucleotide reductase-R2, peroxidase activity in manganese catalases, and hydrocarbon desaturation in stearoyl carrier protein desaturase.[13–16] The shared structural homology within this family, an active site containing two iron atoms housed within a four helix bundle and coordinated by a conserved ligand motif, is likely a product of divergent evolution from a common ancestor.[4,15] BMMs isolated from different bacteria are therefore highly adapted towards utilizing specific hydrocarbons as source of both carbon and energy, while retaining conserved structural features.

The BMM family is also internally diverse. Evolutionary analysis of BMMs delineates subfamilies by substrate preference, which is often correlated with similar macromolecular protein structure.[4] Relevant subfamilies include soluble methane monooxygenases (sMMOs), four component alkene/aromatic monooxygenases or toluene monooxygenases (TMOs), phenol hydroxylases (PHs), αβ alkene monooxygenases (AMOs), hyperthermophillic toluene monooxygenases (SsoMOs), and tetrahydrofuran/propane monooxygenases (THMOs).[1,4,14,17–20] Broadly, sMMOs and other three-component monooxygenases convert a wide variety of small

hydrocarbons to their respective alcohols (Figure 1).[1,3,21,22] In contrast, TMOs, PHs and other subfamilies preferentially hydroxylate aromatic systems or epoxidize alkenes with high regiospecificity, although sMMO can act on these substrates as well.[1,19,20,23,24]

Well characterized members of sMMO and TMO families, soluble methane monooxygenase (sMMO) and toluene / o-xylene monooxygenase (ToMO), exemplify this diversity in reaction chemistries. sMMO has been extensively studied for its ability to activate the relatively inert C-H bond in methane at ambient conditions, one of the hardest reactions in nature.[1,14,25] TMOs, in particular T4MO, can demonstrate extreme regiospecificity towards aromatics such as toluene or phenol, often yielding product distributions with greater than 90% preference for a given constitutional cresol or catechol isomer. Yet, despite sharing a highly conserved tertiary and active site structure with sMMO, TMOs and other BMM family members are extremely ineffective at hydroxylating alkanes.[12,24,26] This combination of conserved structure but varied substrate specificity and reactivity suggests catalytic activity depends partially on the unique tuning of the catalytic diiron center by each BMM protein scaffold. The nature of this interaction is highly complex and poorly understood, and may involve a combination of changes in the electronic properties of the diiron center during catalysis and positional or conformational adjustments in the primary and secondary coordination sphere.[1,22,27]

Hence, this study aims to determine the structural origin for differences in substrate specific reactivity of ToMO and sMMO by probing how the protein scaffold surrounding the active site tunes the reactivity of the diiron core. In probing the intrinsic structure-function relationship between coordinating ligands, the metal center, and overall enzymatic activity we hope to assemble a more comprehensive understanding of how BMMs function. Given the increased focus on engineering biologically inspired catalysis, we aim to utilize this structural information to generate ToMO variants with novel substrate transformation capabilities, specifically the terminal alkane hydroxylation characteristic of sMMO.

B. Relevant Properties of BMMs

Generally, BMMs require a minimum of three independent protein components for catalysis – an $\alpha_2\beta_2\gamma_2$ hydroxylase housing the diiron center in the α-subunit, an NADH-dependent reductase to reduce the diiron center via electron transfer through FAD and [2Fe-2S] cluster cofactors, and a regulatory protein that modulates the reactivity of the metal center

towards dioxygen and target substrates (Figure 2).[15,17,18,28] TMOs, such as ToMO, require an additional rieske-type protein to mediate electron transfer between the NADH-dependent reductase and the diiron center.[29] In the dynamic catalytic cycle, the assembly and disassembly of multiple complexes between the hydroxylase, reductase, and the rieske proteins leads to a broadly similar mechanism across sMMOs and TMOs. Initial reduction of the hydroxylase (sMMOH or ToMOH) to the diiron (II) state by the reductase component (sMMOR, ToMOF & ToMOC) results in a rearrangement of an iron-coordinating Glu residue and repositioning of an adjacent conserved Asn residue on the surface of the hydroxylase α -subunit. These changes promote release of the reductase and binding of the small regulatory protein (sMMOB, ToMOD), which further alters the protein structure to encourage dioxygen activation, substrate channeling to the active site, and eventual substrate hydroxylation. Presumably, oxidation of the metal center then promotes both regulatory protein and product release, completing the catalytic cycle (Figure 2).[1,14,30,31] While the number components in each BMM family member may differ, the functional role of each component is largely preserved.[14,15] Achieving an understanding of these roles as they relate to each component's structure and activity is required for a comprehensive understanding of BMMs.

1. The Hydroxylase Component

The ~ 250 kDa hydroxylase component, responsible for activation and modification of the C-H bond, has been thoroughly characterized mechanistically and structurally utilizing spectroscopic and biochemical techniques.[1,26,32–34] Crystal structures of ToMOH, T4MOH sMMOH, and PHH in various catalytic states have been solved, and indicate both proteins display a similar global topology consisting of dimerized αβγ heterotrimers assembled from individual α, β and γ subunits (Figure 3).[14,35] Intermolecular contacts between opposing α and β subunits in each heterotrimer allow for dimerization to form an $\alpha_2\beta_2\gamma_2$ protomer.[14,24] While not involved in assembly, the γ subunit is thought to stabilize intra-heterotrimer α-β interactions.[14] The resulting canyon formed between each αβγ heterotrimers is approximately 30-34 Å wide and the binding site of the reductase and regulatory protein – as confirmed by recent crystal structures of these complexes. [22,25,36 37]

Despite poor sequence identity between ToMOH and sMMOH, approximately 20% identity, individual subunit function is effectively conserved. The α-subunit has the highest

sequence identity across all BMM systems consisting of $\alpha_2\beta_2\gamma_2$ hydroxylases, ranging from approximately 20-45%.[1,27] Regions proximal to the metal center, including the conserved four helix bundle, tend to display a conserved topology, while remote regions interacting with the β or γ subunits often have unique folds specific to BMM variants. The γ subunit however is found to vary extensively between certain BMM subfamilies and is nonexistent in others, suggesting a nonessential role in BMM catalytic action.[4,14]

2. The Diiron Center

Each α-subunit of the hydroxylase component contains a carboxylate bridged diiron center located approximately 10-12Å beneath the protein surface, positioned within a conserved four α-helix bundle formed by helices B, C, E and F.[1,3,22] Two of these helices, E and F, lie on the hydroxylase surface and participate in conformational changes resulting from binding of the regulatory protein.[1,22,37] Sequence, spectroscopic, and crystallographic analysis of the active site suggests the structure of the oxidized diiron(III) is similar, if not identical, across multiple uncomplexed BMM hydroxylases (Figure 4).[15] Within the four-helix bundle, a glutamate residue bridges the two iron atoms, while two histidines each coordinate a single iron atom at distal positions.[13,14]

A similar three amino acid coordination motif is present in members of the ferritin-like superfamily.[13,20] However, the remaining ligands differ in position and identity, suggesting dissimilar coordination geometries lead to unique metal center reactivity.[13] In ToMO and sMMO three additional glutamate residues emerging from the interior of the α-helices of the four helix bundle, as well as multiple solvent molecules, complete an octahedral coordination sphere for both iron(III) atoms (Figure 4).[21,28,35] Product binding to the center assumes a bridging positon by displacing solvent molecules, indicating spatial rearrangement of the diiron core is a key component in the catalytic cycle.[17,38]

Considering the differential activities of ToMOH and sMMOH, it is interesting to note both proteins have near identical arrangements of the diiron core when the hydroxylase is in a resting oxidized (H_{ox}) and reduced (H_{red}) state.[17,21,39,40] However, throughout the course of the reaction, as the hydroxylase traverses through various redox states and undergoes conformational changes from interactions with component proteins, the position of key amino acids, such as coordinating glutamate residues, change. As a result, crystallographic and spectroscopic

evidence suggests the T4MOH / ToMOH and sMMOH component bound states and reaction cycle intermediates differ significantly in the arrangement of coordinating ligands.[17,27] A goal of this investigation is to understand the reason for these structural changes as means to identify the structural origin of ToMO's differing activity, as compared to sMMO.

3. Substrate Channeling to the Diiron Center

To carry out substrate hydroxylation, BMM hydroxylases must channel various reactants including dioxygen, electrons, protons and target hydrocarbons into the active site pocket in proximity to metal center.[14,38,41,42] Timing of substrate delivery must be highly regulated to prevent accidental quenching of reactive catalytic intermediates by the surrounding solvent or premature reduction of the metal center.[43] Routes for substrate entry and egress identified in ToMO and sMMO pass through internal cavities or channels oriented from the metal center towards the surface (Figure 5).[1,28] In sMMO, these successive hydrophobic cavities have been found to accommodate haloalkane and alcohol substrates, supporting their role as substrate channels.[44] Residues near each cavity opening are considered to act as gates for substrate access, and may contribute towards substrate specificity.[28] Upon binding of the regulatory protein sMMOB after the diiron center is reduced, changes in helices E and F shift gating residues into 'open' conformations, forming a connected channel that extends to the protein surface.[45] Simultaneously, the position of sMMOB binding occludes a small pore between helices E and F thought to facilitate small molecule exit from the diiron center.[1,14,28,44] This level of regulation, a combination of weakly regulating which carbon-based substrates enter the active site and when other reactants such as dioxygen can exit, may contribute broadly towards sMMO's substrate preference.

Unlike sMMO, ToMO contains a contiguous channel approximately 6-10Å wide and 30-35Å long stretching from diiron center to the protein exterior.[15,17,38] (Figure 5a). The ToMO substrate channel is continuously open in both oxidized and reduced states, suggesting the diiron center is more exposed to external solvents and therefore less likely to achieve long lived catalytic intermediates.[38,43] However, when ToMOD binds to the hydroxylase, likely after the metal center is reduced, the channel entrance is sealed and isolated from the external solvent (Figure 5b).[14,36,46] The large diameter of the channel correlates well with the preference of ToMO for aromatic substrates.[42] A hydrophobic isoluecucine residue and two phenylalanines are found

at the channel's opening to the active site, and are proposed to be gating residues limiting the entry of charged or polar substrates to the diiron center.[38,47] Mutagenesis and recent computational analysis of the active site suggests they may play a role in determining the regiospecificity of hydroxylation.[12,42] Given the requirement for rapid dioxygen activation after substrate entry into the active site pocket, spectroscopic and crystallographic analysis has established cavities analogous to those in sMMOH are responsible for the passage of dioxygen to the reduced diiron center. Subjecting these residues to mutational analysis has confirmed the importance of their hydrophobic character to successful catalysis.[38,48] The differences in substrate access to the diiron center and the mechanisms by which access is regulated explain in part the substrate specificities of ToMO and sMMO, although this does not explain the differences in reactivity toward hydrocarbons.

4. The Reductase and Rieske Proteins

Reduction of the hydroxylase component in TMOs and sMMOs is initiated by a ~47 to 67 kDa NADH-dependent oxidoreductase (sMMOR and ToMOF).[1,14,31] In TMOs and other four-component BMMs an additional ~10 to 12 kDa Rieske protein, (ToMOC) participates in this electron transfer chain.[29,49] The reductase is an iron-sulfur flavoprotein characterized by a N-terminal ferredoxin-like domain containing a [2Fe-2S] iron-sulfur cluster and a C-terminal FAD-containing domain.[24,26,36] As revealed by stopped-flow optical, EPR, and Mössbauer spectroscopy, electrons initially oxidized from an NADH cofactor are utilized to first reduce FAD to $FADH_2$. Subsequent single electron transfer from the reduced hydroquinone to the $[2Fe\text{-}2S]^{3+}$ cluster is then coupled with reduction of either the diiron center in sMMOH, or the Rieske protein ToMOC (Figure 6a,b).[29,31] Structurally, the rieske protein contains a [2Fe-2S] cluster as well, organized within a series of α-helices. With a reduction potential ranging from -150 to -50 mV, current mechanistic understandings suggest the Rieske protein acts to shuttle electrons from ToMOF to ToMOH. In both the TMO and sMMO systems, two successive electron transfers are required to reduce the hydroxylase diiron (III) center to initiate catalysis.[1,29,36] Hence, the reductase component effectively couples electron input into BMM systems with dioxygen activation and substrate hydroxylation.

Evidence also suggests that regulatory protein binding and successful catalysis is partially dependent on changes in the binding epitope related to diiron center reduction.[1] . Both sMMOR

and ToMOC have a high affinity for oxidized sMMOH and ToMOH, respectively, and bind to the α-subunit at the inter-heterotrimer cleft as supported by a recent crystal structure of the T4MOH-T4MOC complex.[22,36,50,51].[37] In sMMO, sMMOB is observed to compete with sMMOR for binding to sMMOH after it has been reduced to the H_{red} state, indicating a change in K_d values after reduction has occurred. Similar behavior is observed in ToMO with ToMOC binding to ToMOH in the H_{ox} state.[36] Hence, the efficiency of electron transfer and component interaction appears critical to catalytic success by effecting various structural changes in the hydroxylase. One characteristic example of this kind of structural change preceding regulatory protein binding to the hydroxylase is a rotamer shift inwards of an externally facing asparagine residue helix E of the α-subunit (Asn 214 in sMMOH and Asn 202 in ToMOH) (Figure 9).[1,22,52,53] The exact effect of this change, present in ToMOH, sMMOH and T4MOH, is unclear.

Further, while the reductase is considered critical for activity in a complete BMM system, various chemical methods utilizing redox active dyes or cryoreduction with an electron beam have often been used to artificially generate the H_{red} and H_{ox} states.[3,15,43] The resulting artificially reduced hydroxylase can still react with dioxygen and substrate to yield hydroxylated product. However, spectroscopic characterization of the reaction pathway followed by artificially reduced hydroxylase demonstrates the absence of a unique colorless catalytic intermediate normally present in the reaction cycle. This suggests that reduction as executed by the reductase component protein regulates in part the nature of the catalytic cycle, likely through induced structural changes in the hydroxylase.[49]

5. The Regulatory Protein

All currently known BMMs require a ~10-12 kDa regulatory protein component essential in regulating catalysis.[1,3,4,14] While ubiquitous, the sequence identity and tertiary structure of these proteins is generally not conserved, even within subfamilies.[4] When complexed with the hydroxylase component, the reactivity of the BMM system increases approximately 20 – 200 fold.[14,25,53,54] Steady state analysis of NADH consumption suggests the regulatory protein binds optimally at a 1:2 ratio to the hydroxylase.[25] Complexation is also known to influence various structural changes that have functional implications, such as spatial shifts in ligands coordinating the iron atoms that differ by BMM subfamily. Of importance, sMMOH complexed with sMMOB displays an accelerated rate of dioxygen activation, efficient coupling of NADH

consumption to substrate to hydroxylation, alteration of the spectroscopic and redox properties of the diiron center, and changes in the regio- and stereospecificity of overall product distributions.[21,22,53] ToMO complexed with its regulatory protein ToMOD displays similar behaviors.[7,12,17] In both sMMOH and ToMOH, regulatory protein binding may cover up a substrate access channel present between helices E and F, which suggests an additional role in determining pathways for dioxygen access to the metal center. Together, especially in the context of the regiospecificity present in ToMO and T4MO, these numerous associated functionalities emphasize the importance of ToMOD and sMMOB in regulating catalysis.[1,54]

The specific regions required for this regulation in sMMOB are the N- and C-terminal domains. Deletion of either domain leads to an inactive system. The N-terminal domain in TMO regulatory proteins does not demonstrate similar behavior, as cleavage results only in decreased binding affinity for the hydroxylase.[45] While not a conclusive analysis, this cursory assessment suggests that in addition to displaying different mechanisms for substrate channeling and different shifts in coordinating ligands after reduction, the diiron cores of both ToMO and sMMO may be activated in fundamentally different ways. Further examination of the specific residues which compose these channel-like structures in ToMO and sMMO is therefore required.

C. Differences in the sMMO and ToMO Catalytic Cycle

It is evident that while BMMs have many conserved structural features, ToMO and sMMO have vastly different reactivity toward different substrates. Evidence directs our attention towards differences in their catalytic cycles. The sMMO catalytic cycle is the most well characterized of different BMs, and serves as a reference for our understanding of a similar cycle displayed by ToMO. From an initial oxidized diiron(III) state, the diiron core is reduced to diiron(II). As a result of this reduction, key coordinating residues in sMMO are observed to undergo positional shifts. Specifically, Glu-243 is observed to shift from monodentate to bidentate chelation of the diiron atoms (Figure 4).[3,15] A similar shift of the analogous Glu-231 residue in ToMO is also observed. In both proteins, the distance between the iron atoms in the active site increases from a conserved 3 Å distance to 3.3 Å in sMMO and 3.4 Å in ToMO (Figure 7). Comparable shifts observed in inorganic analog complexes are established to modify the reactivity of the diiron center within the complex's scaffold.[55,56] Hence, it seems likely these positional ligand changes influence both the sMMO and ToMO reaction pathways. As expected,

spectroscopic determination of sMMO intermediates after reduction indicates catalytic intermediates are both electronically and structurally different between the two proteins (Figure 8).[57,58]

Following reduction and regulatory protein binding, the reduced diiron(II) core activates dioxygen – resulting in a peroxo-coordinating diiron(III) intermediate. Stopped flow UV-Vis spectroscopy of this intermediate, denoted P*, suggests it is a short-lived species forming directly from the decay of H_{red} after dioxygen binding.[21,43,52] A proton transfer step then results in the formation of a similar intermediate between ToMO and sMMO – a peroxodiiron(III) H_{peroxo} species, which absorbs between 700-750 nm in sMMO. The kinetic lifetime of this intermediate decreases in the presence of electron rich substrates in both sMMO and ToMO, leading to its assignment as the hydroxylating intermediate in the catalytic cycle.[21,33]

In sMMO, the H_{peroxo} can react with electron rich substrates to yield hydroxylated products via a two-electron transfer mechanism.[57] However, in the absence of such substrates, O-O bond cleavage and proton transfer lead to a highly reactive di-μ-oxo diiron(IV) intermediate termed Q in which the iron atoms are separated by only 2.6 Å. This intermediate absorbs strongly at 400 nm and actives the inert C-H bond in methane and other alkanes.[59] The exact mechanism by which the diiron core severs the O-O bond is unclear, but increasing evidence suggests proton-assisted heterolytic cleavage facilitated by core ligands such as Glu-243 may be responsible.[1] Extended decay of Q in the absence of substrate yields a nonreactive Q* state, identified by stopped-flow UV-Vis spectroscopy. Because this state decays rapidly to form H_{ox} the exact function of this state is unclear.[1,21,53]

Although sMMO has a slower turnover rate than ToMO for their respective substrates, formation of intermediate Q and subsequent conversion of methane to methanol is relatively rapid, ranging from 0.25-2s^{-1} and 2.9-3.9s^{-1} respectively.[1] The mechanism for Q-mediated C-H hydroxylation is another source of speculation. Recent work supports a radical-based mechanism dependent on a the 'diamond core' conformation which places high valence iron atoms in close proximity to substrate and activated oxygen.[59] Interestingly however, quantum DFT calculations are unable to yield this diiron conformation *in silico*.[1]

The H_{peroxo} intermediate in ToMO is associated with significantly different Mössbauer parameters than $sMMOH_{peroxo}$, suggesting dioxygen activation of the reduced diiron center leads to differing geometries.[1,33,49] While a conserved μ-1,2 peroxodiiron species may be possible,

rapid freeze quench Mössbauer characterization indicates the diiron centers in this state assumes a μ-1,2 conformation with the activated dioxygen occupying an 'end on' bridging position (Figure 8, Model 3).[21,60] The exact nature of this structure remains unclear, and comparison of Mössbauer parameters to those of model compounds has led to multiple models for H_{peroxo} diiron center organization (Figure 8).[1,14]

Unlike $sMMOH_{peroxo}$, $ToMOH_{peroxo}$ is unable to decay to a Q-like intermediate. Instead, $ToMOH_{peroxo}$ may decay through two different pathways – either forming hydrogen peroxide (H_2O_2) by hydroxylation of solvent molecules, or producing alcohols through hydroxylation of aromatic and other electron rich substrates. In both cases, the return to H_{ox} after product release proceeds without a high valent diiron(IV) intermediate characteristic of sMMO.[1,14,24,26,61] Mechanistically, an inability to achieve this intermediate Q explains why ToMOH is unable to hydroxylate alkanes. This allows us to refocus our main investigation towards determining the structural origins of ToMO's inability to form a diiron(IV) intermediate, and engineering a variant capable of accessing one.

Advances towards this goal have followed from computational analyses of the ToMOH active site pocket. Through this methodology, which has involved DFT calculations and Monte-Carlo minimization of potential intermediates, a nonessential but highly conserved threonine residue was observed to dictate the kinetic stability of the H_{peroxo} intermediate in ToMOH.[27,34] The methyl group of Thr-201 locks the residue's hydroxyl group in a position that promotes hydrogen bonding with a simulated peroxo intermediate. In sMMO, the analogous residue Thr-213 is too far away to achieve similar stabilization. Hence, when this conformational lock is removed by mutation of Thr-201 to serine in ToMOH, two intermediates are found to accumulate – one closely matching the $ToMOH_{peroxo}$ diiron(III) intermediate, the other displaying optical and Mössbauer parameters similar to $sMMOH_{peroxo}$.[15,27,33] However this new intermediate displays similar decay patterns as $ToMOH_{peroxo}$ including increased catalytic activity towards aromatics, indicating an equilibrium between the two species – however, there is no pathway by which the $sMMOH_{peroxo}$ -like intermediate in this ToMOH T201S variant can convert to Q.[33] Work in the Sazinsky lab to replicate this mutant has confirmed the increased rate of turnover.[62] Similar turnover rate increases are observed in a few T4MO Thr-201 mutants.[39]

One explanation for this, based on modelling of the interaction between Thr-201 and the diiron center, predicts the Thr-201 hydrogen bond increases the energy barrier of a $ToMOH_{peroxo}$

to Q transition by approximately 4.7 kcal / mol by stabilizing the $ToMOH_{peroxo}$ intermediate.[27] In conversion of threonine to serine, and removal of the rotational barrier which ensures hydrogen bonding to the intermediate, this barrier is partially removed. This is supported by evidence that the T201A mutation T4MO, which eliminates hydrogen bonding at residue 201, results in faster rates of $T4MOH_{peroxo}$ decay via H_2O_2 production and release.[63]

However, crystal structures of T201S ToMO variants do not demonstrate significant conformational change at this position, possibly as a result of the crystallization process, although this conformation may differ after ToMOD binding.[62] However, under the assumption that a similar conformation-lock is responsible for regulating activity, a cursory survey of the ToMO active site pocket identifies multiple other residues capable of hydrogen bonding to peroxo-intermediate oxygens and therefore stabilize intermediates in a manner similar to Thr-201. This has far reaching implications with respect to the role of hydrogen bonding induced stabilization and rigidity in the active site of ToMO versus sMMO.

D. Why Not Q? Rigidity in the Catalytic Cycle.

1. Active Site Rigidity

In trying to understand why TMOs cannot achieve intermediate Q, motion models of T4MO and sMMO reaction cycle were created using crystal structures of the reduced and oxidized hydroxylases with and without the regulatory protein. In general, residues which participate in successive spheres of hydrogen bonding oriented around the diiron center are observed to move less in T4MOH than in sMMOH. This suggests multiple residues in ToMO, including those directly coordinating the iron atoms, are constrained by hydrogen bonding networks. The primary coordination sphere of this network includes Thr-201, and is highly conserved across multiple BMM subfamilies.[1,14,20] Generally, this network extends ~10-13Å from the two distal diiron-coordinating histidines through the interior of the four-helix bundle towards the intermediary surface region within Helix A (Figure 10). While in ToMO certain residues are replaced by structural water molecules, the general topology of this network is preserved.[1,51] Of note, analogous networks in RNR-R2, rubrethyrin and other ferritin-like superfamily members contain residues required for catalytic activity.[1,13,15,28] This suggests the importance of the network in promoting regulation of the diiron center. Further, due to the

extensive size of the network regulation is likely indirect as residues in the second or third coordination of ToMO or sMMO spheres have been implicated as required for catalysis.

One such example of flexibility in sMMO, but rigidity in ToMO is E104 in ToMO, a monodentate ligand that hydrogen bonds to a glutamine residue Gln-141 approximately 2.8Å away. An analogous residue in sMMO, Glu-114, is 4.2Å from the nearest hydrogen bonding partner Cys-151, and is observed to vary more in conformation when the regulatory protein binds. Similarly, regulatory protein sMMOB binding is observed to broadly induce relaxation of many hydrogen bonds in these spheres.[22,53] An example of this in sMMOH-B is a shift in the position of Gln-140, reducing hydrogen bonding with two coordinating ligands Glu-209 and Glu-144. Similar behavior is not observed in T4MO, where regulatory protein T4MOD binding results in high positional conservation (Figure 10). Taken together, this suggests constraints provided in part by hydrogen bonding in the secondary and tertiary coordination sphere may prevent TMO from accessing a higher valent reactive intermediate Q.

2. Bulk Rigidity

Similar models of protein motion also suggest bulk backbone motions in ToMO are more constrained that in sMMO. That is, residues of approximately the same function and spatial orientation are found to move less in ToMO than in sMMO over the course of the catalytic cycle in general. As has been considered, regulatory protein binding in the catalytic cycle establishes distinct structural changes in ToMO and sMMO. Further examination suggests conformations in ToMO are generally more restricted than in sMMO. For example, many of the residues implicated in the secondary and tertiary coordination spheres are components of helices E and F, within the regulatory protein binding epitope.[36] Included in this group are residues with known roles in catalysis such as Asn-214/Asn-202, which potentially is associated with reductase protein binding,[1,15] and Thr-213/Thr-201, which is theorized to stabilize H_{peroxo} in ToMOH. In sMMOH, sMMOB binding draws Asn214 upwards through an intermolecular contact and partially rotates Thr213 out of the active site (Figure 9). As a result, the α-helix E on which Thr-213 resides is further deformed into a π-helix. Helix F is also observed to tighten, decreasing inter-turn distance. However, in comparison the extent of helix deformation, tightening, and residue motion in general upon ToMOD binding to ToMOH is reduced.[1,22]

Given that the changes sMMOB and ToMOD induce are known to alter the electronic properties of the active site iron atoms, for example decreasing the reduction potential and a shifting the characteristic diiron(II) EPR signal, it is logical to suggest these structural changes are directly influencing the reactivity of the diiron center. This is further supported by magnetic CD spectroscopy measurements indicating the extent of changes in the ligand electronic environment of sMMOH is greater than in ToMOH when complexed with sMMOB and ToMOD respectively.[14] This influence may extend as well to the stabilization or destabilization of specific intermediates or side-reactions in the catalytic cycle. Considering that it is presently unclear whether ToMOD is actually bound when substrate hydroxylation occurs, this is an interesting possibility.

E. Engineering a Novel ToMO capable of Terminal Alkane Hydroxylation

We have reviewed the current understanding of differences in ToMO and sMMO with respect to substrate channeling, active site organization, and interaction with critical component proteins. Reactivity differences seem to arise from the way surrounding ligands and broader protein backbone interact with this core. The sustained interest in engineering BMMs capable of unique substrate transformations implies a more thorough understanding of how these cores function is required. Hence, our investigation proposes to examine why the ToMO metal center cannot carry out C-H bond activation of alkanes by attempting to engineer a variant of ToMO capable of terminal alkane hydroxylation, through modification of the surrounding protein scaffold. Determining which aspects of the center and surrounding scaffold are more relevant than others is crucial to achieving this goal.

With respect to our goal of engineering an intermediate Q in ToMO, this work presents two possible avenues. First, curtailing secondary and tertiary participants in the hydrogen bonding network may decrease structural rigidity in a manner similar to the T201S mutation, eventually leading to a conformation capable of forming the reactive intermediate Q. Alternatively, modifying regions of low mobility to increase flexibility may result in a broader structural change responsible for changing the physical properties metal center into those required for the formation of intermediate Q. Though both are based on an incomplete mechanistic understanding of ToMO and sMMO, results from both avenues can serve to guide further understanding of how the protein scaffold tunes these centers differently.

1. Current Approaches in ToMO Engineering

Previous work in the Sazinsky lab pursuing the first of these hypotheses aimed to reduce constraints on primary sphere residues by mutating secondary sphere residues to non-hydrogen bonding analogs.[64] Building on the T201S mutation that affords ToMO a sMMO-like peroxo intermediate, numerous variants were produced with this strategy [62]

Towards our eventual goal of achieving an intermediate Q in ToMO, this investigation focuses on characterizing the kinetic activity present in these ToMOH variants, including any non-standard activities present. With this kinetic information, we aim to better understand how modifying the coordination sphere within ToMO influences the catalytic activity. In doing so, we also seek to develop new methods for determining regions of high rigidity and identifying potential sites where mutations may increase mobility and allow for the diiron center to enter new catalytic states or support a $ToMOH_{peroxo}$ to Q conversion. To support this analysis, we also seek to optimize current purification and screening procedures to facilitate broad mutational analyses.

By analyzing these second coordination sphere mutants biochemically and structurally, we hope to advance our efforts in engineering terminal alkane hydroxylation in ToMO. This work will hopefully also yield insights into the underlying structure-functional relationship between the diiron core and the surrounding ligand environment which has remained elusive for BMM systems as complex as these.

III. Methods

A. Expression and Purification of ToMOH

BL21(DE3) *E. coli* cells transformed with pET22b(+) / touBEA were grown in LB media adjusted to pH 7. Single colony cultures were grown in media treated with 100 µg/mL ampicillin overnight, then used to inoculate larger batch cultures prepared with the same conditions. Cultures were grown at 37ºC with shaking at 220 rpm to OD_{600} of ~0.6-0.8, then expression induced with 25 µM IPTG at 25ºC. Iron ammonium sulfate solution at a concentration of 100µM in solution was supplemented to ensure an excess of Fe^{+2} in the growth media. Four hours after induction, cells were pelleted at 5000 rpm for 5 min using a Beckman JLA 10.500 rotor and recovered cell pellets flash frozen with liquid nitrogen to assist with cell lysis.

Cell pellets were lysed via sonication. First thawed pellets were dissolved in Buffer A (Buffer A: 25 mM MOPS, 50 mM NaCl, 10% glycerol, 2 mM cysteine, 8 mM thioglycolate, pH 7.0) at a ratio of 3-5 g / mL, then treated with 1 mM $MgCl_2$ and small quantities of DNase and PMSF. Cell slurries were then sonicated in an ice slurry for 6-8 min with 20 second pulses followed by 20 second pauses to prevent denaturation. Cleared lysate was obtained by centrifuging crude lysate at 12,500 rpm at 4ºC for 45-60 min to pellet cell debris. The resulting supernatant was passed through a 0.22μM filter, then loaded onto a DEAE Q-Sepharose Fast Flow packed column (GE Healthcare) previously equilibrated with Buffer A. The column was washed with Buffer A to baseline at a flow rate of 2 mL / min, then ^{57}Fe-ToMOH eluted with Buffer B (Buffer A with 500mM NaCl) in a salt gradient from 50 – 500 mM NaCl over 50 min. The column was washed with Buffer B for an additional 25 minutes to ensure complete elution. Presence of ToMOH in eluted factions was determined via SDS PAGE analysis. Pure fractions with ToMOH, lacking obvious impurities, were recombined and concentrated to a total volume of < 3 mL using 100kDa spin filters (Amicon Ultra).

Second step purification was carried with an improved gel filtration / size exclusion set up, using two in-series Superdex-200 columns packed with Sephadex-200 resin (26 mm x 100 cm). Tandem columns were first equilibrated with Buffer C (Buffer A without cysteine or thioglycolate, with 100 mM NaCl), then sample volumes of < 3 mL were loaded. The tandem column was run at a flow rate of 1.3 mL / min, and ToMOH eluted with good resolution after ~1h. Pure fractions were analyzed via SDS PAGE to confirm relative purity, then pooled appropriately and concentrated using 100kDa spin filters. Protein concentration was estimated using UV-Vis absorbance at 280 nm and the Beer-Lambert Law (ε= 600,000 $M^{-1}cm^{-1}$). Samples were then frozen with liquid nitrogen, and stored at -80ºC for further use.

B. Expression and Purification of ^{57}Fe-ToMOH

Iron-57 enriched ToMOH was expressed and purified as previously described for wild-type ToMOH, with the following modifications: BL21(DE3) *E.coli* cells transformed with pET22b(+) / touBEA were grown in ^{57}Fe-enriched media made by combining casamino acids, nucleotide triphosphates, trace salts (acetate, succinate, chloride, hydroxide and phosphate), trace metals (zinc chloride, cobalt chloride, sodium molybdate, calcium chlorate, borate), vitamins (biotin, folic acid, pyrolidine, thiamine, nicotinic acid, pantothenic acid, para-amino benzoic acid,

thioacetic acid) and $^{57}FeCl_3$, prepared by dissolving ^{57}Fe metal (99.67% isotopically enriched) in concentrated sulfuric acid. This complete media was supplemented with 100 µg/mL carbenicillin for both overnight and batch cultures. Each hour after induction, 100µM $^{57}FeCl_3$ solution was added to growth media to ensure an excess of isotopically enriched $^{57}Fe^{+2}$, until cells were pelleted.

C. Expression and Purification of ToMOH Variants

A library of ToMOH mutants was obtained either through site directed mutagenesis of the pET22b+/touBEA vector, or saturation mutagenesis of the touBEA gene followed by subcloning into the pET22b+/touBEA vector. Mutants were expressed and purified as previously described for wild-type ToMOH with the following modifications: Certain purifications utilized a third step, where ToMOH fractions generated from size exclusion purification were pooled and loaded onto a Phenylsepharose column (26 mm x 40 cm), equilibrated in 1.3 M NaCl, 25 mM MOPS, pH 7.0. and 10% glycerol. Pooled fractions were treated with NaCl to bring the total salt concentration to ~1.3M before loading, and protein was then eluted from the column at a flow rate of 2 mL/min using a salt gradient of 1.3-0.1 M NaCl over 50 min.

D. Expression and Purification of ToMOD

Expression of ToMOD followed from (29). BL21(DE3) *E. coli* cells transformed with pET22b+ touD were inoculated in overnight cultures of LB media containing 100 µg / mL ampicillin, and grown at 37ºC with shaking at 200 rpm. Larger batch cultures supplemented with 100 µg / mL were then inoculated from overnight cultures and grown under the same conditions. At an OD_{600} of ~0.6 – 0.8, cells were induced with IPTG at a final concentration of 500µM and allowed to express for three hours at 25ºC. Cells were pelleted at 5000 rpm for 5 min using a Beckman JLA 10.500 rotor, then froze in liquid nitrogen to assist with lysis.

Cells were lysed with sonication as previously described for ^{57}Fe-ToMOH. Buffer D (25 mM MOPS, 5% glycerol, 1 mM DTT, pH 6.9) was used for lysis instead of Buffer A. Supernatant obtained after centrifugation of crude lysate at 12,000 rpm, 4ºC, 45-60 min was passed through a 0.22 µm filter, then loaded onto DEAE Q-Sepharose Fast Flow packed column (GE Healthcare) previously equilibrated with Buffer D. The column was washed with Buffer D, then ToMOD eluted with Buffer E (Buffer D + 500mM NaCl) in a linear gradient from 0-500

mM NaCl over 80 min. ToMOD presence in eluted fractions was determined via SDS-PAGE, and pure fractions were recombined and concentrated to < 2 mL using 5 and 10 kDa spin filters (Amicon Ultra).

Second step gel filtration / size exclusion purification was carried out using a Superdex-75 column packed with Sephadex-75 resin previously equilibrated in Buffer D. Concentrated ToMOD samples were loaded and eluted within 90 min with good resolution. As described, UV-Vis and SDS PAGE were used to confirm purity and estimate protein concentration (ε= 2980 M^{-1} cm^{-1}). Pure fractions were recombined and concentrated using 10 kDa spin filters. Aliquots of ToMOD were then frozen in liquid nitrogen and stored at -80ºC for further use.

E. Expression and Purification of ToMOC

Expression of ToMOC followed from (23). BL21(DE3) *E. coli* cells transformed with pET22b+ touC were inoculated in overnight cultures of LB media containing 100 μg / mL of ampicillin, and grown at 37ºC with shaking at 210 rpm. Overnight cultures were then used to inoculate larger batch cultures containing 100 μg / μL ampicillin and grown under the same conditions. At a culture OD_{600} of ~0.6 – 0.8, expression was induced at 25ºC with IPTG at a final concentration of 500 μM. Every hour after induction, 100μM of $Fe(NH_4)_2(SO_4)_2 \cdot 6H_2O$ was added to ensure excess iron in media. After 4h of growth, cells were pelleted using a Beckman JLA 10.500 rotor, frozen in liquid nitrogen, and stored at -80ºC to assist with lysis.

Cells were lysed as previously described for ^{57}Fe-ToMOH. Buffer F (25 mM MOPS, 5% glycerol, 10% ethanol, 80 mM NaCl, 2 mM DTT, pH 6.9) was used for lysis instead of Buffer A. Supernatant obtained after centrifugation of crude lysate at 15,000 rpm, 4ºC, 45-60 min was passed through a 0.22 μm filter, then loaded onto DEAE Q-Sepharose Fast Flow packed column (GE Healthcare) previously equilibrated with Buffer F. The column was washed with Buffer F, then ToMOC eluted with Buffer G (Buffer F + 400mM NaCl) in a linear gradient from 0-400 mM NaCl over 150 min. ToMOC presence in eluted fractions was determined via SDS-PAGE, and pure fractions were recombined and concentrated to < 2 mL using 5 kDa spin filters (Amicon Ultra).

Second step gel filtration / size exclusion purification was carried out using two different methods. The first method utilized a Superdex-75 column packed with Sephadex-75 resin previously equilibrated in Buffer F. The second method utilized a Superdex-200 column packed

with Sephadex-200 resin previously equilibrated in Buffer F. For both, concentrated ToMOC samples were loaded and eluted within 80 and 180 min respectively. The Superdex-75 column was found to resolve ToMOC better than the Superdex-200. UV-Vis at 340nm and SDS PAGE were then used to confirm eluted fraction purity and estimate protein concentration (ε= 6870 M^{-1} cm^{-1}). Pure fractions were recombined and concentrated using 5 kDa spin filters. Aliquots of ToMOC were then frozen in liquid nitrogen and stored at -80ºC for further use.

F. Expression and Purification of ToMOF

Purified ToMOF was obtained generously from (62) at high purity after sequential purification by ion affinity and size exclusion chromatography.

G. His-tagging ToMOH and Purification Optimization

1 . Expression and Purification of His-tagged ToMOH

Sequencing of the pET22b+ / touBEA vector containing the recombinant ToMOH gene revealed a potential linker between the α-subunit of the hydroxylase's C-terminus and an in-frame 6X his-tag. Site directed mutagenesis was carried out to remove a stop codon preventing terminus-tag fusion by a third party (Genewiz). BL21(DE3) cells were then transformed with this modified vector, and His-tagged ToMOH was expressed as previously described for wild-type ToMOH with the following modification: growth media was supplemented with an excess of iron ammonium sulfate during induction to account for 6X his-tag presence. Cell pellets were then separated into 2.50 g aliquots and lysed separately to facilitate a series of buffer optimization trials aimed at increasing purification yield.

Crude lysates were purified via Immobilized Affinity Metal Chromatography (IMAC) using either a single or double NiNTA 5 mL HisTrap Fast Flow column (GE Healthcare) after column equilibration with the relevant trial buffer. Trial buffers are presented in Table 1. Samples were eluted from the column with an instantaneous gradient to 500mM imidazole, and protein-containing fractions identified via a UV-Vis detection at 280 nm as well as SDS PAGE. Pure fractions were recombined and concentrated as well as buffer-exchanged with Buffer C using 100kDa spin-filters (Amicon), then stored at -80ºC. Recovery efficiency was estimated by comparing relative yield in eluted versus flow-through fractions, as determined by SDS PAGE analysis.

2. Reconstitution of Apo *Hydroxylase*

Apo ToMOH was made anaerobic by repeated purging with N_2 gas under vacuum within an anaerobic chamber. A reconstitution buffer containing 100 mM MOPS, 100 mM NaCl, and 5% glycerol at pH 7.0 as well as a stoichiometric amount of iron ammonium sulfate was made anaerobic by purging with N_2 gas for 10 minutes, then added to apo ToMOH within the anaerobic chamber. Final concentrations in solution of ToMOH and iron(II) were 50 μM and 200 μM respectively. Apo hydroxylase was incubated with reconstitution buffer for 1–3h on ice in anaerobic conditions, then diluted and buffer-exchanged with ~50 mL Buffer C using a 100kDa spin filter (Amicon) to remove excess iron. Purified samples were then analyzed for iron content, and subsequently frozen and stored at -80ºC.

H. Protein Characterization

1. Determination of Protein Concentration

Concentrations of ToMO components were determined through UV-Vis spectroscopy at 280 nm, as well as at additional wavelengths as required. Molar extinction coefficients specific to each protein were utilized, as previously determined in the literature. In cases where molar extinction coefficients were not available, they were calculated using the online tool ExPASY. (http://web.expasy.org/protparam/)

2. Ferrozine Assay

The presence of iron in protein samples was detected via a colorimetric assay using ferrozine reagent. Complexation of Fe^{2+} and ferrozine in solution yields a colored compound which absorbs strongly at 562 nm. A standard curve was constructed by generating standards consisting of varying concentrations of Fe^{2+} and a standard buffer (300 mM acetate / 100 mM tartrate, 10 mM ferrozine reagent, 75 mM ascorbate, 2 M guanidine HCl). Iron concentrations ranged between 0 – 110 μM. After mixing by inversion, standards were incubated at room temperature for 5 minutes to allow for complex formation. A zero-iron standard was used as a control. Absorbance of standards at 562 nm was measured using a Beckman UV-Vis spectrophotometer in cuvettes with a consistent path-length. Samples of ToMOH to be assayed were prepared by mixing 5μL, 10 μL or 20 μL of protein solution with standard buffer, followed

by heating to facilitate protein denaturation. In cases of high protein concentration, up to 100 µL of concentrated nitric acid was added to facilitate protein degradation, with compensatory changes in buffer levels. Additionally, the concentration of guanidine was increased to 6-8 M to facilitate dissolution. Absorbance at 562 nm was then measured as done for the standards. Iron concentration in an assay sample was determined using a linear relationship between absorbance and concentration derived from standard curve construction, followed by back-calculation to account for sample dilution.

I. Activity Assays

1. Coupled Assay for Aromatic Hydroxylase Activity

The ability of the full ToMO system, consisting of ToMOH, ToMOC, ToMOF and ToMOD, to convert phenol to catechol was examined utilizing a coupled assay with Catechol-2,3-dioxygenase (C2,3O) as a measure of ToMOH activity (Figure 14a). In brief, rapid cleavage of aromatic substrate catechol by C2,3O to form the colored product 2-hydroxymuconic semialdehyde (ε_{410nm} = 12620 M^{-1} cm^{-1}) allows for kinetic monitoring of ToMOH mediated conversion of phenol to catechol. Relevant wild-type and mutant ToMO variants were assayed at 25ºC utilizing this method, and product conversion recorded as a function of absorbance at 410 nm. Relevant experimental parameters are provided in Table 2. Initial rates of product, formation and hence catechol production, for each variant were determined by nonlinear least-squares regression of time course absorbance measurements, utilizing the R language and the statistics package MASS, followed by differentiation of the fit model and evaluation at t = 0. The average RMSD of these fits was 0.036. Rate measurements were then averaged, and the mean initial rate of hydroxylation determined in units of activity (U), specifically micromoles of product produced per minute per milligram of protein (µmol / min / mg).

2. Coupled Assay for Determining Peroxidase Activity

A coupled assay for peroxidase activity was adapted from the previously described assay for hydroxylase activity, utilizing H_2O_2 instead of NADH as a reaction substrate (Figure 14b). Wild-type and mutant ToMOH variants were assayed at various H_2O_2 concentrations ranging from 800µM to 200 mM, as well as in the presence and absence of C2,3O. Relevant experimental parameters are presented in Table 3. Average rates of peroxidase activity were then

determined in units of activity (U) as previously described for the coupled assay for hydroxylation.

3. NADH Consumption Assay

Data relating to the consumption of NADH with respect to the production of catechol collected by (62) and (64) was re-analyzed to determine an approximate ratio of hydroxylase activity to NADH consumption. Relevant experimental parameters associated are present in Table 4.

4. H_2O_2 Quantification Assay

A colorimetric assay utilizing acidified $TiOSO_4$ was developed to quantify levels of H_2O_2 in aqueous solutions. In the presence of H_2O_2, acidified $TiOSO_4$ reacts to form a colored perititanic acid complex that absorbs strong at 407 nm (Figure 14c). Initial assay design was adapted from previous protocols.[65,66] Acidified $TiOSO_4$ detection reagent solution is prepared by diluting 0.05 g / mL acidified $TiOSO_4$ reagent (Fischer) in ddH_2O with concentrated sulfuric acid in a 1:4 v/v ratio. Detection reagent is then heated to 35ºC for 1h to facilitate mixing and dissolution. Optimization of assay parameters was carried out, and various solutions of acidified $TiOSO_4$ detection reagent were reacted with H_2O_2 samples of known concentration to determine a combination ratio yielding a linear response with good sensitivity. Out of multiple ratios examined, a 1:2 ratio of detection reagent to sample solution was found to meet these criteria. Standard curves were then constructed to relating known quantities of H_2O_2 to absorbance in solution at 407 nm to determine assay reproducibility and effective detection limits. Standards were prepared in quintuplicate by combining H_2O_2 solutions in pH 7.5 phosphate buffer with ddH_2O, and detection reagent in a 1:2 v/v ratio. Absorbance measurements were carried out using a 96-well plate and fluorescence plate reader (HiTek) at 407 nm, with 50 µL sample volumes per well. Where appropriate, solutions were further diluted to yield an absorbance measurement less than 2.0 AU.

5. Assaying for H_2O_2 Decomposition.

Utilizing the H_2O_2 quantification assay, the H_2O_2 decomposition activity of ToMOH Wt, mutant ToMOH variants, and bovine liver catalase was determined discontinuously. Specifically,

at various time-points, individual reactions between relevant catalase-active proteins and peroxide were treated with $TiOSO_4$ detection reagent in a 1:2 v/v ratio and concentrated sulfuric acid in a 1: v/v ratio, and absorbance at 407 nm determined. Kinetic assays at various concentrations of peroxide were carried out in multiplicate (3-7x) in 50mM Phosphate buffer at pH 7.5 and absorbance measurements determined using a 96-well plate and fluorescence plate reader (HiTek) at 407 nm, with 50 µL sample volumes per well. Relevant experimental parameters are presented in Table 5. Where required, solutions were further diluted to yield a measurable absorbance. For reactions analyzing the kinetics of enzyme catalase, data was collected at time-points spaced by 5 second intervals. For analysis of ToMOH and ToMOH variants, data was collected at time-points spaced at 30 second intervals.

The resulting time-course absorbance measurements were converted to concentrations utilizing a standard curve prepared as previously described, and initial rates of substrate consumption determined by either nonlinear least squares regression followed by model differentiation and evaluation at t = 0, or linear approximation in the first 10 seconds. When applicable, initial rate measurements across various peroxide concentrations were then fit to a model for Michaelis-Menten kinetics, and relevant kinetic parameters determined.

6. Assaying for Superoxide Dismutase Activity

Wild-type and mutant ToMOH variants were assayed for their ability to generate H_2O_2 while in solution. Purified hydroxylase was first treated with potassium ferricyanide to deplete any peroxide initially present in solution, then buffer exchanged with Buffer C and concentrated utilizing 100kDa spin filters (Amicon). Hydroxylase in Buffer C at an approximate concentration of 1 µM was then incubated at room temperature or 4ºC in the presence or absence of a stoichiometric amount of ToMOD (2 µM). The concentration of H_2O_2 in solution was then determined at time-points at t = 0 and t = 24h utilizing the previously described assay for quantifying H_2O_2 in solution. Superoxide activity rates were then calculated as the difference in peroxide concentrations between time-points.

J. Analysis of Backbone and Residue Rigidity of ToMOH and sMMOH

The bulk rigidity of ToMO and sMMO were determined through a novel analysis based on examining how the spatial positions of backbone and residue atoms vary between crystal

structures obtained of these proteins in various states of their catalytic cycles. Where crystal structures of ToMO catalytic states could not be obtained, T4MO crystal structures were utilized.

Crystal structures of ToMOH and sMMOH in H_{ox}, H_{ox}-Reg, and H_{red}-Reg states were obtained, and corrected for mistakes in atom assignment, residue identity, and positional variance. Linear interpolation and energy minimization techniques utilizing the CNS Solve software suite (version 1.30) were then applied to generate smooth 'morphs' consisting of 90 'frames' of ToMOH and sMMOH transitioning through these various states in the following order: oxidized, component bound, reduced (sMMO PDB IDs: 1MTY, 1FYZ, 4GAM, T4MO PDB IDs: 3DHG, 4P1C, 3DHI). Atomic positions of backbone and residue atoms were then extracted, and subjected to two forms of analysis. First, for each protein, variance in interatomic distance between each individual atom and the bulk protein structure across all 'frames' of the morph was calculated, and the mean of this variance for each atom was reported. This metric is denoted as the mean positional variance. Second, for each protein, differences in atomic position between each 'frame' for each single atom were calculated as a proxy for the spatial derivative of atomic position with respect to time, and the mean of this degree of positional change reported. This metric is denoted the mean spatial derivative. Bulk rigidity was then determined using these two metrics. Across similar atoms, defined as those which share < 5 Å difference in position between sMMO and ToMO, the mean variance in interatomic distance and mean change in atomic position were examined and compared. Processing of coordinate datasets was carried out using custom scripts within the following environments: Python 3.6 with the numerical analysis packages Numpy, Scipy, and Biopython, Matlab (R2016a. Mathworks), and PyMOL (versions 1.71 and 1.3, Schrodinger). Relevant code can be accessed through a github repository associated with this work (http://github.com/asnanda/).

IV. Results

This work sought to investigate the kinetic behavior of ToMOH variants developed with the intent of engineering sMMO-like terminal alkane hydroxylation in ToMO. To this extent, wild-type and mutant variants were obtained through overexpression and purification, and characterized through a range of kinetic techniques. Additionally, further steps were made improving methods for screening for differences in kinetic behavior, as well as determining key structural intermediates in the ToMO catalytic cycle. A structural and computational analysis of

the role of rigidity in the catalytic cycle was also carried out, lending support to the direction currently pursued towards developing an alkane-hydroxylating ToMO.

A. Expression and Purification of Wild-type ToMO, ToMO Variants, and ToMO Component Proteins

Wild-type ToMO hydroxylase was successfully overexpressed and purified as described with good yield, in the range of 30-33 mg of protein per liter growth media. The previous three-step purification process utilized by (62) was reduced to a faster two-step process by doubling the size of the size exclusion column, which yielded better hydroxylase separation and resolution. Ferrozine assay determination of iron content indicated Wild-type ToMOH batches had greater than 3.5 iron atoms per dimer, close to the expected 4.0 iron atoms per dimer.

ToMOH variants were obtained either through overexpression and purification in the same manner as wild-type ToMOH, or from stocks generated in a similar manner. Mutants were also found to have greater than 3.5 iron atoms per dimer.[62,64] In total, seven variants of ToMOH, three single mutants and four double mutants, were obtained and utilized in this work. Each sample was found to be relatively pure through SDS-PAGE analysis, and acceptable for further use.

Component proteins ToMOC, ToMOD, and ToMOF were also successfully obtained, either through overexpression and purification following established methods or from prior stocks generated and purified through similar means. Specifically, overexpression and purification ToMOC and ToMOD were carried out, while ToMOF was obtained generously from (62). In general, component proteins were obtained at high purity acceptable for further use (Figure 12).

B. Determining the Structure of $ToMOH_{peroxo}$

In collaboration with the Solomon Group at Stanford, we sought to study the catalytic cycle of ToMOH by NRVS (Nuclear Resonance Vibrational Spectroscopy) which would - facilitate the identification and characterization of the $ToMOH_{peroxo}$ intermediate structure. Wild-type ToMO hydroxylase was prepared with Iron-57 to yield isotopically enriched diiron centers detectable via Mössbauer spectroscopy. Enriched hydroxylase was generated through overexpression of wild-type ToMOH in BL21(DE3) cells grown in an isotopically enriched

growth media, and purified following the established methodology (Figure 11). Protein aliquots established by UV-Vis spectroscopy to contain minimal contaminants after two-step purification were recombined and concentrated to approximately 2.43 mM diiron centers, as determined by ferrozine assay. Two diiron centers were assumed per hydroxylase, resulting in a protein concentration of approximately 1.2 mM. This purified Iron-57 enriched ToMOH and ToMOD at a stoichiometrically equivalent concentration (~ 29 mM) were provided to the Solomon Group to first carry out Rapid Freeze-Quench Mössbauer, to identify samples with significant quantities of intermediate, and then characterize the frozen samples with trapped intermediate by NRVS with the goal of determining the structure of the $ToMOH_{peroxo}$ intermediate. Work is currently ongoing, and results are expected within the year.

C. His-Tagging ToMOH and Purification Optimization

To develop an efficient system for the rapid screening and purification of ToMO mutants, a variant of wild-type ToMOH with a 6X his-tag attached at the C terminal of the α-subunit was generated, and purification optimized. The 6X his-tagged construct was generated by Genscript by mutating the stop codon present on the 3' end of the touA gene within the touBEA pET22b+ plasmid such that an in-vector 3 amino acid linker and His-tag were appended.

The pET22b+/touBEA-his vector was successfully transformed into BL21(DE3) cells, and overexpressed following the same methods utilized for wild-type ToMOH. Expression yields obtained were lower than for wild-type, approximately 18-20 mg protein per L media as compared to 30 – 33 mg protein per L media. However, ~2L growths were observed to consistently result in good expression.

His-tagged ToMOH was purified using IMAC columns attached to an FPLC system (Figure 13). Various purification conditions were trialed in order to optimize his-tagged ToMOH recovery and purity, as determined by gel quantification of SDS PAGE analysis of eluted fractions. In general, across all buffers, purification was found to result in highly pure samples equivalent to wild-type ToMOH purified via a three-step affinity purification process, within only 10-25 minutes – a significant reduction from the length multistep process. Phosphate buffers lacking imidazole with low salt at pH 7 resulted in greatest recovery, approximately 70%. Of note, across all buffers pH conditions approaching 7 resulted in the greatest yield. This differs from the expected pH 8.0 normally seen in IMAC related purifications. Protein was also found to

precipitate rapidly from phosphate solution due to high concentration in eluted fractions, and hence required immediate buffer exchange into any MOPS based buffer with < 10% glycerol.

Concentrated his-tagged ToMOH displayed negligible aromatic hydroxylase activity, as well as minimal iron content as determined by ferrozine assay, suggesting the IMAC purification processes removes the iron from the active site of ToMOH. Purification with buffers containing Iron(II), thioglycolate and cysteine did not increase ToMOH iron content, or return aromatic hydroxylation activity. Samples were therefore reconstituted with iron(II) to determine whether activity could be recovered. Building on previous work, a reconstitution protocol was developed.[14] When applied, reconstituted His-ToMOH was relatively active, capable of hydroxylating aromatic compounds with nearly 66% the activity of wildtype. However, iron (II) content as determined by ferrozine assay was approximately 4-12 atoms per dimer hydroxylase, significantly greater than the expected 4 per dimer, indicating poor removal of extra iron after reconstitution.

D. Activity Assays

1. Assay for Aromatic Hydroxylase Activity

Wild-type ToMO and mutant ToMO variants were assayed for their ability to hydroxylate an aromatic substrate as a means of assessing whether the studied mutations altered baseline enzymatic activity. The ToMO system was reconstituted in full for each variant, and an initial product formation rate determined from time-course measurements of catechol production over a relevant time-frame. Predominantly, the mutations studied in this work were found to significantly alter reaction rate as compared to wild-type ($p < 0.001$ for relevant mutants) (Figure 15). Of single mutants, the T201S mutation yielded a ~3-fold activity enhancement over wildtype, 168.5 ± 0.5 versus 55.7 ± 0.3 U respectively, while E104D resulted in a ~ 2-fold slower hydroxylation activity, 25.6 ± 8.3 versus 55.7 ± 0.3 U respectively. Subsequent mutations on the T201S backbone resulted in double mutants displaying extremely low activities in general, with the exception of the E214G mutant which was not found to alter activity in either single or double mutant conditions. Of particular interest, E111 mutants displayed similar degrees of activity reduction, suggesting the importance of the E111 position. Similarly, the Q141C mutation appears to completely inhibit aromatic hydroxylase activity, implying Q141 plays a key role in catalysis.

Estimated ratios of NADH coupling, comparing the rate of NADH consumption to product formation, were not found to correlate strongly with mutated residue properties. All T201S double mutants displayed reduced coupling as compared to wildtype, with E111A/T201S and E111N/T201S mutants displaying similarly reduced ratios, 0.08 and 0.13 respectively versus 0.38 for the wild-type enzyme. E104D however demonstrated an increased coupling ratio nearly ~ 2-fold greater than wild-type, although a similar increase in aromatic hydroxylase activity was not observed. This analysis assumes a single turnover of product requires a single molecule of NADH. This is not necessarily the case, and thus the validity of these measurements as a means of determining efficiency of substrate consumption is questionable.

2. Assay for Peroxidase Activity

To determine whether ToMOH or ToMOH variants could utilize hydrogen peroxide as an electron and O_2 source, assays for specifically the hydrogen peroxide mediated conversion of phenol to catechol were performed. Due to time constraints, only mutants E104D, E111A/T201S and E111N/T201S were assayed, as well as wildtype. In general, across all variants peroxidase activity was not observed – measurement error was significantly greater than estimated initial rate measurements indicating nonsignificant results (Figure 16). This implies that in ToMO or ToMO variants, a peroxide-shunt cannot be used to initiate catalysis. These findings stand in contrast to the T4MO system, where low peroxide-shunt activity has been demonstrated for aromatic substrates.[51]

However, E111A, E111N and E104D samples displayed significant bubble formation upon incubation peroxide for at least 1 min, in the presence of all other ToMO component proteins. These bubbles were interpreted as the formation of O_2 gas in solution at peroxide concentrations as high as 200 mM. Wild-type ToMOH displayed similar behavior at a reduced magnitude. To confirm activity was derived from the ToMO system, the assay was repeated in the absence of C2,3O and other components. Similar results were observed.

3. Assay for Superoxide Activity

E104D, E111A, E111N and Wt. hydroxylases were further assayed to determine whether they could produce hydrogen peroxide in solution, which may decompose by another reaction pathway to yield O_2 gas. After incubation in hydrogen peroxide-free buffered solutions for 24h,

independent hydroxylase did not appear to produce hydrogen peroxide (Figure 16b). The presence of ToMOD did not influence this behavior, indicating these mutants do not demonstrate a reaction pathway involving peroxide generation.

4. Assay for Catalase-like H_2O_2 *Decomposition Activity*

Based on evidence suggesting ToMOH double mutants E111A / T201S and E111N / T201S and single mutants E104D can decompose hydrogen peroxide in the presence of the fully reconstituted ToMO system, the ability of each variant hydroxylase to break down peroxide was investigated. Utilizing a novel assay capable of detecting hydrogen peroxide concentrations in solution as low as 400 nM, the kinetics of hydroxylase mediated H_2O_2 decomposition were investigated discontinuously. To provide a baseline measure of catalase activity the kinetic behavior of bovine liver catalase at various peroxide concentrations was determined. When fitted to a Michaelis-Menten model of kinetics, the relevant kinetic parameters were determined to be: k_{cat} of 266 s^{-1} and K_m of 272 μM (Figure 17d).

Due to time constraints, H_2O_2 decomposition activity was predominantly examined at 25 mM and 50mM H_2O_2 between the E111A/T201S variant and wildtype. Initial rates of substrate consumption derived from nonlinear least squares fitting of time-course kinetic data indicated the E111A / T201S double mutation demonstrated a near equivalent rate of H_2O_2 breakdown as compared to wild-type (Figure 18a, b, e). However, while wild-type ToMOH appeared to exit a linear kinetic phase within the first 30s, the E111A/T201S variant remained in a linear phase until nearly 90 seconds after reaction initiation. Hence, while wild-type appears to undergo inactivation after consuming hydrogen peroxide as a substrate, the E111A/T201S variant appears to resist this inactivation for longer. The amount of hydrogen peroxide required before the wild-type protein is inactivated is inconsistent between different treatments of hydrogen peroxide, suggesting a secondary, likely nonspecific reaction may be responsible for inhibiting catalase-like activity. The lack of inhibition in the E111A/T201S variant suggests the rate of this side-reaction is reduced as a result of the E111A mutation.

Given that this catalase-like activity was initially observed in a fully reconstituted ToMO system, we sought to determine whether interaction between the regulatory protein and the hydroxylase could influence the rate of hydrogen peroxide decomposition. When incubated with ToMOD in a 1:2 stoichiometric ratio, both the wild-type and E111A/T201S variants displayed

decreased initial rates (Figure 18e). For wild-type ToMOH, the rate of hydrogen peroxide decomposition was repressed nearly 9-fold in the presence of ToMOD. Additionally, wild-type ToMOH treated with ToMOD appeared to exit the linear kinetic phase more rapidly, as compared untreated wild-type enzyme (Figure 18d). The E111A/T201S mutant demonstrated a lower rate-reduction, ~6 fold, but maintained linear decomposition kinetics, indicating a consistent resistance to peroxide-mediated inactivation (Figure 18c). Hence, this resistance appears to be responsible for the qualitative increase in bubbling observed when assaying ToMO variants for peroxidase activity as it remains a conserved feature of the E111A/T201S mutant hydroxylase in the presence and absence of the ToMO regulatory protein.

E. Analysis of Rigidity in sMMO and ToMO

Previous qualitative analyses of crystal structures of ToMOH and sMMOH have indicated that key residues near the active site as well as whole regions of the protein bulk differ in position between oxidized, reduced, and component bound states. We sought to develop a method for quantifying the degree of this mobility through the use of linear-interpolation models of protein, or 'morphs'. For the purpose of providing a higher quality analysis, T4MO was utilized in place of ToMO. Morphs generated for T4MOH and sMMOH resulted in a sample of 90 individual simulated structures based off of the crystal structures of T4MOH and sMMOH hydroxylase α-subunits in key catalytic states– oxidized, reduced, and component bound. Utilizing positional information of backbone atoms in both T4MOH and sMMOH, rigidity was assessed with two metrics – mean change in atomic position and mean variance in interatomic distances for each atom. Both metrics and plotted with respect to atomic position as a means of comparing between proteins.

In general, the α-subunit of sMMOH displays a significantly increased mobility score as compared to that of T4MOH, with a mean positional variance of 0.103 versus 0.047 respectively (Figure 20). This ~2-fold difference is evident when comparing mobility across all backbone atoms, with sMMOH demonstrating approximately seven clustered regions of increased mobility, as compared to three in T4MOH. Interestingly, while on average the α-subunit of sMMOH is more mobile, there are approximately four regions of overlap where both proteins share similar degrees of mobility. When the 20 percent most mobile atoms are indicated on the structures of the α-subunits of T4MOH and sMMOH, this similarity becomes clear, predominantly in regions

of helices E and F (Figure 20c). However, unique mobile regions in T4MOH and sMMOH are also present and are relevant for further study.

To further compare the two structures, a spatial alignment of α subunits of T4MOH and sMMOH generated a set of 429 residues which were determined to be spatially identical within a distance < 5Å. For each equivalent residue in each protein, both the mean positional variance and mean spatial derivative were computed by averaging these metrics across the individual atoms composing each residue. Interestingly, the motional behavior of these residues was similar to that of the backbone in both enzymes, with regions of high and low mobility conserved between these two samples (Figure 21a, b). When analyzing the distribution of the mean positional variance in both enzymes across all equivalent residues, the highest frequency of values was observed at 2^{-3} Å in sMMOH and 2^{-4} Å in T4MOH, indicating that residues in the α subunit of sMMOH are ~2 fold more mobile (Figure 21c). In order to identify residues with high differential mobility, residue mobility in T4MOH was plotted with respect to mobility in sMMOH. In general, while a small sample of residues displayed an approximately 1:1 relationship, the majority of equivalent residues were high mobile in sMMOH and rigid in T4MOH, or vice versa (Figure 22a). Residues which were on average more highly differentially mobile in sMMOH were extracted, and mapped to the α subunit of T4MOH in order to determine relevant regions. As opposed to the surface E and F helices implicated via backbone analysis, a large number of highly differentially mobile equivalent residues were located in the interior of T4MOH, within the four-helix bundle and in proximity to the diiron center (Figure 22b). The twenty-five most highly mobile are presented in Table 8. Additionally, smaller subsections of small hinge-like helices were also identified as differentially mobile, suggesting the way in which the broader protein scaffold 'flexes' may also differ between sMMOH and T4MOH.

V. Discussion

A. Rigidity Analysis and Evidence of Rigidity in the Catalytic Cycle:

The initial hypothesis guiding the generation of various second-sphere mutants suggested constraints applied to residues participating in the extensive hydrogen bonding network present in ToMOH prevented the diiron center from assuming a ligand geometry required to achieve a Q-like intermediate. By modifying residues and regions contributing to this rigidity, conformational locks on the diiron active site could be reduced.

Individual analysis of the crystal structures of ToMOH and sMMOH in the oxidized, reduced and component bound states suggested qualitatively that residues participating in the hydrogen bonding network in sMMOH as well as in the larger protein scaffold were more mobile than in ToMOH. Through generation of motion models based on these crystal structures and subsequent analysis of changes in atomic position through the reaction cycle, the backbone of the α-subunit of sMMOH was determined to be on average nearly twice as mobile as the backbone of the α-subunit of T4MOH. Additionally, T4MOH demonstrated fewer regions of increased mobility as compared to sMMOH.

Because ToMOH and T4MOH have a high sequence identity, 68%, and extremely similar structures in oxidized and reduced states, it is valid to extend this result to ToMOH. In supporting this hypothesis, this analysis also allows for determining unique regions of both ToMOH and sMMOH that are highly mobile. Regions meeting this criteria over the course of the catalytic cycle were predominantly in helices near the diiron center. Unique features were identified in T4MOH and sMMOH, and represent regions which require further study.

Of the shared regions determined to be highly mobile in both T4MOH and sMMOH, the most predominant feature is a two-helix motif predicted as the binding site for ToMOD and sMMOB component proteins (Figure 20). The importance of this region has already been studied with respect to the definitive structural changes resulting from regulatory component interaction. Further, this region is also implicated in less well-understood structural changes associated with diiron center reduction and reductase component binding. While it is not surprising this region would be identified as mobile in sMMO, it is notable that in T4MOH, it is the most mobile region. This suggests the majority of positional changes in the T4MO backbone over the course of the catalytic cycle are related to the interaction of T4MO with component proteins, predominantly the regulatory protein.

However, when comparing spatially equivalent residues, the majority of residues that are highly mobile in sMMOH but rigid in T4MOH are located within the T4MOH α-subunit interior, in proximity to or within the four-helix bundle. Additionally, these residues are observed to cluster together in regions that are either negligibly or partially mobile in T4MOH. In theory, this supports our original hypotheses that closely associated residues participating in the secondary coordination sphere may be constrained in ToMOH versus sMMOH. In practice, this provides a series of future targets for mutational analysis. The twenty-five most differentially mobile

residues presented in Table 8, as well as the helices E and F implicated through analyzing and comparing backbone mobility, represent regions of future interest. The importance of these helices with respect to binding the regulatory protein ToMOD, and the direct importance of four-helix bundle residues in catalysis, suggests mutations to these regions may be critical in releasing constraints on the metal center, allowing for the formation of high-energy reactive intermediates.

B. Characterization of the Kinetic Activities of ToMO Variants

In general, second sphere ToMOH mutants displayed reduced aromatic hydroxylation activity, with the exception of the well characterized T201S variant, implying the importance of network-participating residues in promoting successful catalysis. The T201S mutation, which has been discussed for its removal of a conformational lock on the diiron center in ToMO homologs, yields a similar rate enhancement in ToMO as in ToMO homologs. Together, these results suggest alteration of the hydrogen bonding network can directly influence the reactivity of the diiron center.

Rate enhancements or decreases were not necessarily correlated with ratios of NADH coupling. Coupling efficiencies were found to vary significantly from that of wild-type ToMO for all variants, but in general second sphere mutants showed decreased coupling. Interestingly, the mutant E104D was found to be ~2 fold less active but ~2 fold more efficient with respect to NADH coupling than wildtype, indicating a lower activity may not always be correlated with reduced coupling. However, in contrast, the more active T201S variant had a lower coupling efficiency than wild-type. Thus, it seems that while changes in coupling efficiency are a feature of modifications to the diiron enter, they do not always reflect changes in aromatic hydroxylation activity.

Access to nonstandard reaction pathways and potentially unique intermediates was also observed amongst ToMOH variants. In mutants E104D, E111N / T201S and E111A / T201S, the appearance of catalase-like decomposition of H_2O_2 was determined to occur at the same initial rate as wild-type enzyme, but to resist peroxide-mediated inactivation to a significantly greater degree than wild-type. This resistance allows ToMOH variants to decompose hydrogen peroxide for a longer kinetic lifetime than wild-type ToMOH, indicating mutations to these secondary coordination sphere residues favor an alternate reaction pathway that is normally inhibitory. Hence, we suggest wild-type ToMOH is undergoing a form of catalytic inactivation through

reaction with hydrogen peroxide decomposition products, such as the OH radical. The ability of this radical to modify residues in proximity to the active site and inactivate catalase-like enzymes has already been demonstrated. [67] This modification, if occurring, does not appear to be consistent, as different quantities of peroxide are consumed in the 25 mM and 50 mM treatments before inactivation is observed. The time until inactivation also seems to decrease when wild-type ToMOH is incubated with ToMOD, while similar incubation of E111A/T201S with ToMOD does not alter the mutant's peroxide-inactivation resistance. ToMOD mediated reduction of activity in wild-type supports the hypothesis that catalase-like activity is a side reaction ideally suppressed in the normal catalytic cycle. Further investigations into the nature of this inactivation, and the resistance displayed by these secondary coordination sphere mutants, is therefore warranted. In particular, determining whether inactivated wild-type and mutant ToMOH retains hydroxylase activity will help inform whether inactivation is associated with the modification or breakdown of key active-site residues.

In contextualizing these results, we note that weak catalase-like activity has been previously reported in ToMO homologs T4MO and T2MO.[25,51] In ToMO, similar activity initially observed in a fully reconstituted system was determined to result from contaminants. However, the independent hydroxylase at high purity has never been examined. Hence, the appearance of this activity in Glu-111 and Glu-104 variants purified via the modified procedure described in this work suggests that reducing conformational constraints on the diiron core by removing hydrogen bond stabilization of key primary ligands results in increased preference for an alternate reaction pathway.

Specifically, a structural water molecule coordinated by Glu-134 is determined to be absent in recently solved recently solved crystal structures of the E111N / T201S mutant, and E104D in wild-type ToMO is partially coordinates the diiron center directly. It is possible changing the hydrogen bonding network topology at either of these positions is correlated with increasing the preference for reactive interactions between the diiron core and hydrogen peroxide.

It is important to understand as well the mechanistic basis of catalase and peroxidase activity in ToMO and BMMs in general. It has been shown that $ToMOH_{peroxo}$ in a fully reconstituted system decays in the absence of substrate to generate H_2O_2 and a return to the H_{ox} state in the context of a fully reconstituted ToMO system. An initial consideration would suggest catalase-like activity in ToMO is this reaction in reverse, with H_2O_2 binding to a diiron(III)

species such as $ToMOH_{ox}$, then rapidly generating a peroxodiiron(III) species without the necessary reduction or dioxygen activation steps facilitated by ToMOC, ToMOF and ToMOD respectively.[68] This alternative mechanism, denoted as a 'peroxide shunt', is present in a variety of BMMs and nonheme oxygenase enzymes such as sMMO, T4MO, adenine deaminase and cytochrome P450.[25,57,69,67] For example, while sMMO does not generate hydrogen peroxide in H_{peroxo} decay, fully reconstituted sMMO systems can efficiently utilize H_2O_2 as an oxygen and electron source for substrate hydroxylation. The exact mechanism supporting this activity is unclear – H_2O_2 may react with either a reduced diiron(II) metal center or bind an oxidized diiron(III) metal center. The result however is an equivalent product distribution and catalytic rate as the full system.[25] Similarly, in both the presence and absence of the regulatory protein T4MOD, T4MOH displays an extremely inefficient peroxidase pathway with significantly decreased regiospecificity.[51] Whether this is correlated with the bulk changes in rigidity of the catalytic cycle determined here remains a point of further investigation. Crystallographic evidence from these experiments suggests H_2O_2 interaction with a reduced diiron(II), but no known intermediates are detectable with UV-Vis spectroscopy in the course of the reaction cycle.[51]

Given these established peroxidase pathways in the highly homologous T4MO, it is interesting that wild-type ToMO or any of the variants studied in this work do not display peroxidase activity as either a single hydroxylase component or a fully reconstituted system, despite demonstrating closely interrelated catalase-like activity. Attempts to initiate peroxidase activity with ToMOD, ToMOH, ToMOC, hydrogen peroxide and substrate resulted instead in further catalase-like H_2O_2 decomposition and O_2 release.[43,58]

Recent work in examining the redox properties of inorganic analogs of the BMM metal center have yielded evidence that diiron(III) complexes with near-equivalent coordination arrangements to ToMO can achieve a diiron(IV) oxidation state through reaction with hydrogen peroxide.[32] Hence, activating a peroxide shunt pathway in ToMO may present a viable method for achieving a high-valent intermediate in a modified ToMO variant. The theoretical interrelation between the peroxide shunt pathway and H_2O_2 decomposition in BMMs implies that further mutation of ToMO variants displaying catalase-like activity may present a first step towards engineering a protein capable of generating an sMMO-like H_{peroxo} intermediate capable of converting to Q and hydroxylating alkanes. [60] Further, engineering this shunt pathway would

represent a fundamental change in the mechanism of ToMOH catalysis that may provide strong insights into the differential stability of catalytically active H_{peroxo} like states.

C. A Structural Basis for Differing Peroxide-related Activities

At present however, it is difficult to establish how exactly E111N / T201S and E111A / T201S or E104 mutants are contributing towards a reaction pathway that favors H_2O_2 decomposition. In part, this is because the geometry of the $ToMOH_{peroxo}$ state is not known. As has been discussed, spectroscopic evidence that the $ToMOH_{peroxo}$ intermediate differs from the $sMMOH_{peroxo}$ intermediate indicates the two species are fundamentally different at a structural level (Figure 8). While efforts to determine the structure of H_{peroxo} presented in this work are ongoing, results are yet to be obtained. Therefore, any analysis of how the hydrogen bonding network in ToMO or ToMO variants may determine the appearance of various catalytic intermediates is necessarily limited. Nonetheless, based on related evidence of H_2O_2 interactions in ToMO analogs, we can speculate how different structural features may result in unique diiron center – peroxide interactions as a means of explaining ToMOs differing peroxide reactivity.

Crystal structures of the T4MOH-D complex soaked with H_2O_2 suggest changes in active site configuration may be responsible for this difference. In T4MOH, peroxide is found in a cis μ-1,2 bridging position, the same as the expected geometry of an $sMMOH_{peroxo}$ like intermediate. Peroxide binding following T4MOD association is also found to induce shifts in residues known to be constrained in ToMOH such as Thr-201and E104, as well as introduce an additional structural water molecule that can h-bond to Fe-atom coordinating residue Glu-231. Further, Glu-231 does not appear to undergo the change in chelation mode normally observed in the H_{red} state and conserved across the majority of BMMs, from monodentate to bidentate.[51]

It is possible that wild-type ToMOH does not experience the same conformational changes upon H_2O_2 binding, and hence does not display peroxidase activity, due protein-specific active-site rigidity. While in general T4MOH is considered to be more rigid, local rigidity in ToMOH may prevent ligand rearrangements similar to those occurring in T4MO, resulting in a different geometry of H_2O_2 binding to the metal center and preference for a different reaction pathway. This is supported by crystal structures of ToMOH soaked with azide or hydrogen peroxide which show both molecules binding the metal center in a μ–η^2,η^2 side-on interaction rather than μ-1, 2 geometry.[17,70] One possible consideration suggests binding in this position in

ToMO or T4MO is favored over the cis μ-1,2-geometry present in T4MOH and sMMO, both of which display catalase-like activity, as hydrogen peroxide displaces a labile hydroxide ion possibly allowing for partial stabilization by hydrogen bonding interactions with Glu-231 and Thr-201. In contrast, mutant Glu-111 ToMOH variants with reduced conformational strain may allow for alternative peroxide binding positions and ligand rearrangements that favor increased formation of $sMMOH_{peroxo}$ like intermediates.[51,52] Further analysis of the crystal structures of azide or hydrogen peroxide soaked ToMOH and T4MOH is required.

The side on binding position H_2O_2 may assume in ToMO closely matches predictions for how hydrogen peroxide may bind the metal center in the H_2O_2 decomposition mechanism observed in two non-heme manganese catalases from the ferritin superfamily - LPC, and TTC from the bacteria *Thermus thermophiles*.[16] Both enzymes bear strong similarity to the active site of ToMO, displaying a conserved metal center and ligand assembly within a four-helix bundle (Figure 23a). In the course of H_2O_2 breakdown, both LPC and TTC enter into divalent Fe(III)Fe(IV) states. Similar states have been achieved in sMMO and ToMO variants, but are not natural intermediates in the catalytic process.[1] Nonetheless, a key aspect of the mechanism in LPC and TTC is two-electron reduction and oxidation of the metal core after hydrogen peroxide side-on binding.[16] Adapting a similar mechanism to ToMO suggests a diiron(III) species initiates H_2O_2 decomposition by oxidizing H_2O_2 to dioxygen and reducing the metal center. The resulting diiron(II) species, with an unknown geometry, can then reduce H_2O_2 to water (Figure 23b). This is a distinct departure from the proposed peroxide shunt mechanism of sMMO and T4MO, which seems to disfavor direct binding to a diiron(III) species like H_{ox}.[25,58]

The importance of this proposed mechanism lies in peroxide-bound hydroxylase traversing through an H_{peroxo} like intermediate in the course of H_2O_2 decomposition, which Glu-111 ToMOH variants potentially access more frequently as a result of increased catalase activity. If this is determined to be the case, then further mutations modifying the second coordination sphere may facilitate the formation of a high valent Q-like intermediate, which may be utilized in a peroxide shunt like pathway. With this theoretical basis for how a peroxide shunt in ToMO may lead to alkane hydroxylating activity, we propose engineering this shunt in ToMO is the next step towards achieving the overall goal of this work while providing strong insights into how different H_{peroxo} intermediates can be generated.

D. Developing a Platform for Rapid Screening for Nonstandard Variant Activity

A key component of the mutational analysis approach employed in this work is the expression, purification and identification of ToMOH variants that display relevant or interesting catalytic activities. Previously, the process of generating pure protein from a given genetic touBEA construct was lengthy and limited the number of mutants which could be generated in an effective time-scale. With the new his-tagged variant of ToMOH, the time required to process and obtain an individual variant in high yield is greatly reduced, averaging a single day from cell lysis to completion. The required reconstitution process to recover catalytic activity necessitates further optimization, but at present results in acceptable baseline levels of aromatic hydroxylation activity.

With the target of engineering a peroxide shunt pathway in ToMO, and new regions proposed for mutation, we hope to leverage this more efficient purification processes along with new assays for H_2O_2 decomposition to rapidly screen for mutants with increased catalase-like activity. We anticipate an increase in the depth of mutant libraries required to achieve this result, and affinity purification, with commercially available tools, facilitates multiplexing this purification process.

The use of the his-tagged ToMOH construct has additional benefits in the production of apo protein. Apo hydroxylase can be reconstituted with a variety of metals to determine how activity varies by core metal properties or with isotopically enriched iron-57 to allow for the analysis of reaction cycle intermediates via spectroscopic techniques. In rapidly generating multiple batches of protein at a small scale, many of these experiments can be conducted in a preliminary fashion to increase the rate at which candidate mutations are identified for further study. Together with new assays for peroxide-related activities, this presents a path forward in the determinate of further mutations required to engineer a peroxide shunt, and eventually terminal alkane hydroxylation, in ToMO.

VI. Conclusions

The goal of this work was to analyze second sphere mutants and assess whether changes in the connectivity of the hydrogen bonding network could reduce conformational locks on the diiron enter, and allow ToMO to access higher level states in the catalytic cycle capable of terminal alkane hydroxylation. Through an analysis of residue and backbone mobility in the

catalytic cycle of sMMO and ToMO, we have found support that differential rigidity in bulk and active-site proximal residues in the two proteins may be responsible for their differing activities. While aromatic hydroxylation activity was found to decrease in mutants designed to reduce this rigidity, specific mutations at E111/T201 and E104 demonstrated a novel increase in catalase-like activity. While incubation with regulatory protein decreased this activity in both wild-type and mutant ToMOH variants, mutant variants demonstrated resistance to the peroxide-mediated inactivation observed in wild-type hydroxylase. The appearance of this activity, as well as resistance to inactivation, after modification of the hydrogen bonding network suggests the formation of intermediates which may be similar in nature to the H_{peroxo} state, resulting from diiron core interaction with peroxide species. While similar peroxide-diiron core interactions in other BMMs, such as sMMOH, can be used to initiate catalysis of relevant substrates, similar peroxidase behavior was not observed.

In comparing BMMs with peroxide shunts to ToMO, it appears that shunt behavior may allow diiron centers to access reactive hydroxylating intermediates, including sMMO Q-state like structures. We therefore propose further mutational analysis aimed at reducing rigidity as a means to engineer a peroxide shunt in ToMO, and potentially generate intermediates capable of terminal alkane hydroxylation. Critical to this is developing a further understanding of the $ToMOH_{peroxo}$ state and how it differs from other BMMs. Results from our collaborative investigation into this difference are forthcoming.

Future work towards this goal requires a dual approach. First, for constraining residues identified as highly differentially mobile in sMMOH, a more detailed analysis of the hydrogen bonding network topology in ToMOH is required to determine which are viable for mutagenesis. Second, selected residues should be mutated such that they retain biochemical properties but lose hydrogen bonding abilities, and the resulting mutant variants further screened for increased catalase activity which may indicate the formation of a high energy peroxo-diiron intermediate that may facilitate access to a Q-like state. We present this as a potential pathway towards achieving terminal alkane hydroxylation in ToMO, and further understanding how the differing activities of sMMO, ToMO and other BMMs can arise from a highly-conserved protein scaffold.

VII. Acknowledgements

This work is supported by the Pomona College Departments of Chemistry and Biology through the Molecular Biology Program, as well as by the Beckman Foundation Beckman Scholars Program. I would first like to thank Professor Matthew Sazinsky for his mentorship, patience and a strong belief in the capabilities and skills of undergraduate students. I would like to thank Professor Rou-jia Sung for her guidance in both life and the lab, and for always reminding me that research is a process, not an endpoint. I would also like to thank Kim Ona-Ayala for her dedicated efforts, building on foundational work done by Lily Zhuang and Anika Burrell in the past years. To my mother for her tireless and thankless efforts to inspire my passions, to my father, grandmother and grandfather for their constancy and love, thank you.

VIII. References

(1) Dubois, J. L.; Ojha, S. *Sustaining Life on Planet Earth: Metalloenzymes Mastering Dioxygen and Other Chewy Gases*; Kroneck, P. M. H., Sosa Torres, M. E., Eds.; Metal Ions in Life Sciences; Springer International Publishing: Cham, 2015; Vol. 15.

(2) Leahy, J. G.; Batchelor, P. J.; Morcomb, S. M. *FEMS Microbiology Reviews*. 2003, pp 449–479.

(3) Merkx, M.; Kopp, D. A.; Sazinsky, M. H.; Blazyk, J. L.; Muanͤller, J.; Lippard, S. J. *Angewandte Chemie - International Edition*. WILEY-VCH Verlag GmbH August 3, 2001, pp 2782–2807.

(4) Notomista, E.; Lahm, A.; Di Donato, A.; Tramontano, A. *J. Mol. Evol.* **2003**, *56* (4), 435–445.

(5) Chauhan, S., Barbieri, P. & Wood, T. K. *Appl. Environ. Microbiol* **1998**, *64* (8), 3023–3024.

(6) Kejriwal, A.; Bandyopadhyay, P.; Biswas, et al. *Dalt. Trans.* **2015**, *44* (39), 17261–17267.

(7) Vardar, G.; Wood, T. K. *Appl. Environ. Microbiol.* **2004**, *70* (6), 3253–3262.

(8) Peters, M. W.; Meinhold, P.; Glieder, A.; Arnold, F. H. *J. Am. Chem. Soc.* **2003**, *125* (44), 13442–13450.

(9) Meinhold, P.; Peters, M. W.; Hartwick, A.; Hernandez, A. R.; Arnold, F. H. *Adv. Synth. Catal.* **2006**, *348* (6), 763–772.

(10) Mccormick, M. S.; Sazinsky, M. H.; Condon, K. L.; Lippard, S. J. *J. Am. Chem. Soc.* **2006**, *128* (47), 15108–15110.

(11) Brouk, M.; Nov, Y.; Fishman, A. *Appl. Environ. Microbiol.* **2010**, *76* (19), 6397–6403.

(12) Notomista, E.; Cafaro, V.; Bozza, G.; Donato, A. Di. *Appl. Environ. Microbiol.* **2009**, *75* (3), 823–836.

(13) Lundin, D.; Poole, A. M.; Sjöberg, B. M.; Högbom, M. *J. Biol. Chem.* **2012**, *287* (24), 20565–20575.

(14) Sazinsky, M. H. **2004**.

(15) Sazinsky, M. H.; Lippard, S. J. *Acc. Chem. Res.* **2006**, *39* (8), 558–566.

(16) Whittaker, J. W. *Arch. Biochem. Biophys.* **2012**, *525* (2), 111–120.

(17) Sazinsky, M. H.; Bard, J.; Di Donato, A.; Lippard, S. J. *J. Biol. Chem.* **2004**, *279* (29), 30600–30610.

(18) Pikus, J. D.; Studts, J. M.; Mcclay, K.; Steffan, R. J.; Fox, B. G. *Biochemistry* **1994**, *36* (31), 9283–9289.

(19) Bertoni, G.; Martino, M.; Galli, E.; Barbieri, P. *Appl. Environ. Microbiol.* **1998**, *64* (10), 3626–3632.

(20) Ji, Y.; Mao, G.; Wang, Y.; Bartlam, M. *Front. Microbiol.* **2013**, *4* (March), 58.

(21) Tinberg, C. E.; Lippard, S. J. *Biochemistry* **2009**, *48* (51), 12145–12158.

(22) Rudd, D. J.; Sazinsky, M. H.; Lippard, S. J.; Hedman, B.; Hodgson, K. O. *Inorg. Chem.* **2005**, *44* (13), 4546–4554.

(23) Murray, L. J.; García-Serres, R.; Naik, S.; Hanh Huynh, B.; Lippard, S. J.; Garcı, R.; Naik, S.; Huynh, B. H.; Lippard, S. J. *J. Am. Chem. Soc.* **2006**, *128* (Figure 2), 7458–7459.

(24) Cafaro, V.; Scognamiglio, R.; Viggiani, A.; Izzo, V.; Passaro, I.; Notomista, E.; Dal Piaz, F.; Amoresano, A.; Casbarra, A.; Pucci, P.; Di Donato, A. *Eur. J. Biochem.* **2002**, *269* (22), 5689–5699.

(25) Gassner, G. T.; Lippard, S. J. *Biochemistry* **1999**, *38* (39), 12768–12785.

(26) Cafaro, V.; Izzo, V.; Scognamiglio, R.; Notomista, E.; Capasso, P.; Casbarra, A.; Pucci, P.; Di Donato, A. *Appl. Environ. Microbiol.* **2004**, *70* (4), 2211–2219.

(27) Bochevarov, A. D.; Li, J.; Song, W. J.; Friesner, R. A.; Lippard, S. J. *J. Am. Chem. Soc.* **2011**, *133* (19), 7384–7397.

(28) Whittington, D. A.; Lippard, S. J. *J. Am. Chem. Soc.* **2001**, *123* (5), 827–838.

(29) Ferraro, D. J.; Gakhar, L.; Ramaswamy, S. *Biochemical and Biophysical Research Communications*. 2005, pp 175–190.

(30) Scognamiglio, R.; Notomista, E.; Barbieri, P.; Pucci, P.; Dal Piaz, F.; Tramontano, A.; Di Donato, A. *Protein Sci.* **2001**, *10* (3), 482–490.

(31) Mason, J. R.; Cammack, R. *Annu. Rev. Microbiol.* **1992**, *46*, 277–305.

(32) Xue, G.; Fiedler, A. T.; Martinho, M.; Münck, E.; Que, L. *Proc. Natl. Acad. Sci. U. S. A.* **2008**, *105* (52), 20615–20620.

(33) Song, W. J.; Behan, R. K.; Naik, S. G.; Huynh, B. H.; Lippard, S. J. *J. Am. Chem. Soc.* **2009**, *131* (17), 6074–6075.

(34) Song, W. J.; McCormick, M. S.; Behan, R. K.; Sazinsky, M. H.; Jiang, W.; Lin, J.; Krebs, C.; Lippard, S. J. *J. Am. Chem. Soc.* **2010**, *132* (39), 13582–13585.

(35) Rosenzweig, A. C.; Brandstetter, H.; Whittington, D. A.; Nordlund, P.; Lippard, S. J.; Frederick, C. A. *Proteins Struct. Funct. Genet.* **1997**, *29* (2), 141–152.

(36) Liang, A. D.; Lippard, S. J. *Biochemistry* **2014**, *53* (47), 7368–7375.

(37) Acheson, J. F.; Bailey, L. J.; Elsen, N. L.; Fox, B. G. *Nat. Commun.* **2014**, *5*, 5009.

(38) Song, W. J.; Gucinski, G.; Sazinsky, M. H.; Lippard, S. J. *Proc. Natl. Acad. Sci. U. S. A.* **2011**, *108* (36), 14795–14800.
(39) Pikus, J. D.; Mitchell, K. H.; Studts, J. M.; McClay, K.; Steffan, R. J.; Fox, B. G. *Biochemistry* **2000**, *39* (4), 791–799.
(40) Fox, B. G.; Froland, W. A.; Dege, J. E.; Lipscomb, J. D. *J. Biol. Chem.* **1989**, *264* (17), 10023–10033.
(41) Bailey, L. J.; Acheson, J. F.; McCoy, J. G.; Elsen, N. L.; Phillips, G. N.; Fox, B. G. *Biochemistry* **2012**, *51* (6), 1101–1113.
(42) Notomista, E.; Scognamiglio, R.; Donadio, L. T.; Pezzella, A.; Di Donato, A.; Izzo, V. *Appl. Environ. Microbiol.* **2011**, *77* (15), 5428–5437.
(43) Murray, L. J.; Naik, S. G.; Ortillo, D. O.; García-Serres, R.; Lee, J. K.; Boi, H. H.; Lippard, S. J. *J. Am. Chem. Soc.* **2007**, *129* (46), 14500–14510.
(44) Lee, S. J.; Mccormick, M. S.; Lippard, S. J.; Cho, U.-S. *Nature* **2013**, *494*.
(45) Wang, W.; Liang, A. D.; Lippard, S. J. *Acc. Chem. Res.* **2015**, *48* (9), 2632–2639.
(46) Liang, A. D.; Wrobel, A. T.; Lippard, S. J. *Biochemistry* **2014**, *53* (22), 3585–3592.
(47) Kurt, C.; Sönmez, B.; Vardar, N.; Yanık-Yıldırım, K. C.; Vardar-Schara, G. *Appl. Microbiol. Biotechnol.* **2016**, *100* (17), 7599–7609.
(48) Fishman, A.; Tao, Y.; Rui, L.; Wood, T. K. *J. Biol. Chem.* **2005**, *280* (1), 506–514.
(49) Liang, A. D.; Lippard, S. J. *J. Am. Chem. Soc.* **2015**, *137* (33), 10520–10523.
(50) Barker, K. D.; Eckermann, A. L.; Sazinsky, M. H.; Hartings, M. R.; Abajian, C.; Georganopoulou, D.; Ratner, M. A.; Rosenzweig, A. C.; Meade, T. J. *Bioconjug. Chem.* **2009**, *20* (10), 1930–1939.
(51) Bailey, L. J.; Fox, B. G. *Biochemistry* **2009**, *48* (38), 8932–8939.
(52) Schwartz, J. K.; Wei, P. P.; Mitchell, K. H.; Fox, B. G.; Solomon, E. I. *J. Am. Chem. Soc.* **2008**, *130* (22), 7098–7109.
(53) Wallar, B. J.; Lipscomb, J. D. *Biochemistry* **2001**, *40* (7), 2220–2233.
(54) Mitchell, K. H.; Studts, J. M.; Fox, B. G. *Biochemistry* **2002**, *41* (9), 3176–3188.
(55) Minier, M. A.; Lippard, S. J. *Dalton Trans.* **2015**, *44* (41), 18111–18121.
(56) Sousa, S. F.; Cerqueira, N. M. F. S. A.; Brás, N. F.; Fernandes, P. A.; Ramos, M. J. *International Journal of Quantum Chemistry*. October 5, 2014, pp 1253–1256.
(57) Lee, S. K.; Nesheim, J. C.; Lipscomb, J. D. *J. Biol. Chem.* **1993**, *268* (29), 21569–21577.
(58) Murray, L. J.; García-Serres, R.; Naik, S.; Hanh Huynh, B.; Lippard, S. J. .
(59) Banerjee, R.; Proshlyakov, Y.; Lipscomb, J. D.; Proshlyakov, D. A. *Nature* **2015**, *518* (7539), 431–434.
(60) Han, W.-G.; Noodleman, L. *Inorg. Chem.* **2008**, *47* (8), 2975–2986.
(61) McClay, K.; Fox, B. G.; Steffan, R. J. *Appl. Environ. Microbiol.* **2000**, *66* (5), 1877–1882.
(62) Ayala, K. O. Engineering Terminal Alkane Hydroxylation in Toluene/ o-xylene Monooxygenase, Pomona College, 2016.
(63) Elsen, N. L.; Bailey, L. J.; Hauser, A. D.; Fox, B. G. *Biochemistry* **2009**, *48* (18), 3838–3846.
(64) Burrel, A. Engineeering Terminal Alkane Hydroxylation in Toluene / o-xylene Monooxygenase, Pomona College, 2013.
(65) Eisenberg, G. *Ind. Eng. Chem. Anal. Ed.* **1943**, *15* (5), 327–328.
(66) Stanford, G. L. Graves Lab H2O2 quantification protocol with TiOSO4 http://www.graveslab.org/lab-resources/procedures/peroxide-h2o2-quantification.
(67) Kamat, S. S.; Holmes-Hampton, G. P.; Bagaria, A.; Kumaran, D.; Tichy, S. E.; Gheyi, T.; Zheng, X.; Bain, K.; Groshong, C.; Emtage, S.; Sauder, J. M.; Burley, S. K.; Swaminathan, S.; Lindahl, P. A.; Raushel, F. M. *Protein Sci.* **2011**, *20* (12), 2080–2094.
(68) Kurahashi, T. *Inorg. Chem.* **2015**, *54* (17), 8356–8366.
(69) Joo, H.; Lin, Z.; Arnold, F. H. *Nature* **1999**, *399* (6737), 670–673.
(70) Lu, S.; Sazinsky, M. H.; Whittaker, J. W.; Lippard, S. J.; Mo??nne-Loccoz, P. *J. Am. Chem. Soc.* **2005**, *127* (12), 4148–4149.

Enzyme	Reaction type	Catalytic reaction	Metabolic role(s)
Methane Monooxygenase (MMO)	Hydroxylation	Fe^{2+}- Fe^{2+} + CH_4 + O_2 → Fe^{3+}- Fe^{3+} + CH_3OH/H_2O	Carbon fixation, methane metabolism
Alkene monooxygenase (AMO)	Epoxidation	Fe^{2+}- Fe^{2+} + RCH=CH_2 + O_2 → Fe^{3+}- Fe^{3+} +  + H_2O	Alkene metabolism
Xanobacter alkene monooxygenase (XAMO)	Epoxidation	Fe^{2+}- Fe^{2+} + CH_3CH=CH_2 + O_2 → Fe^{3+}- Fe^{3+} + 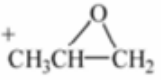 + H_2O	Propene metabolism
Phenol hydroxylase (PH)	Oxidation	Fe^{2+}- Fe^{2+} + 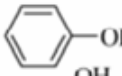 + O_2 → Fe^{3+}- Fe^{3+} + 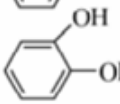 + H_2O	Phenol degradation
Toluene-2-monooxygenase (T2MO)	Oxidation	Fe^{2+}- Fe^{2+} + 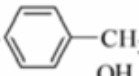 + O_2 → Fe^{3+}- Fe^{3+} + 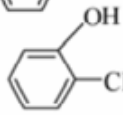 + H_2O	Toluene oxidation
Toluene-4-monooxygenase (T4MO)	Oxidation	Fe^{2+}- Fe^{2+} + 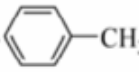 + O_2 → Fe^{3+}- Fe^{3+} + 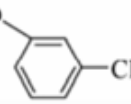 + H_2O	Toluene oxidation
Toluene/*o*-Xylene monooxygenase (ToMO)	Hydroxylation	Fe^{2+}- Fe^{2+} + 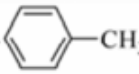 + O_2 → Fe^{3+}- Fe^{3+} +  + H_2O	Toluene, *o*-xylene hydroxylation

Figure 1: *Substrate Transformations of the Bacterial Multicomponent Monooxygenase Family***.** BMM family members display a wide range of chemistries in the conversion of aliphatic, aromatic, and alkene substrates into their respective alcohols. Well characterized sub-families include methane monooxygenases (MMOs), alkene monooxygenases (AMOs), phenol hydroxylases (PHs), and toluene monooxygenases (TMOs). Subfamilies may be distinguished based on substrate preference, with TMOs displaying strong substrate specificity and product regiospecificity as compared to MMOs, which have broad hydroxylation capabilities.[15]

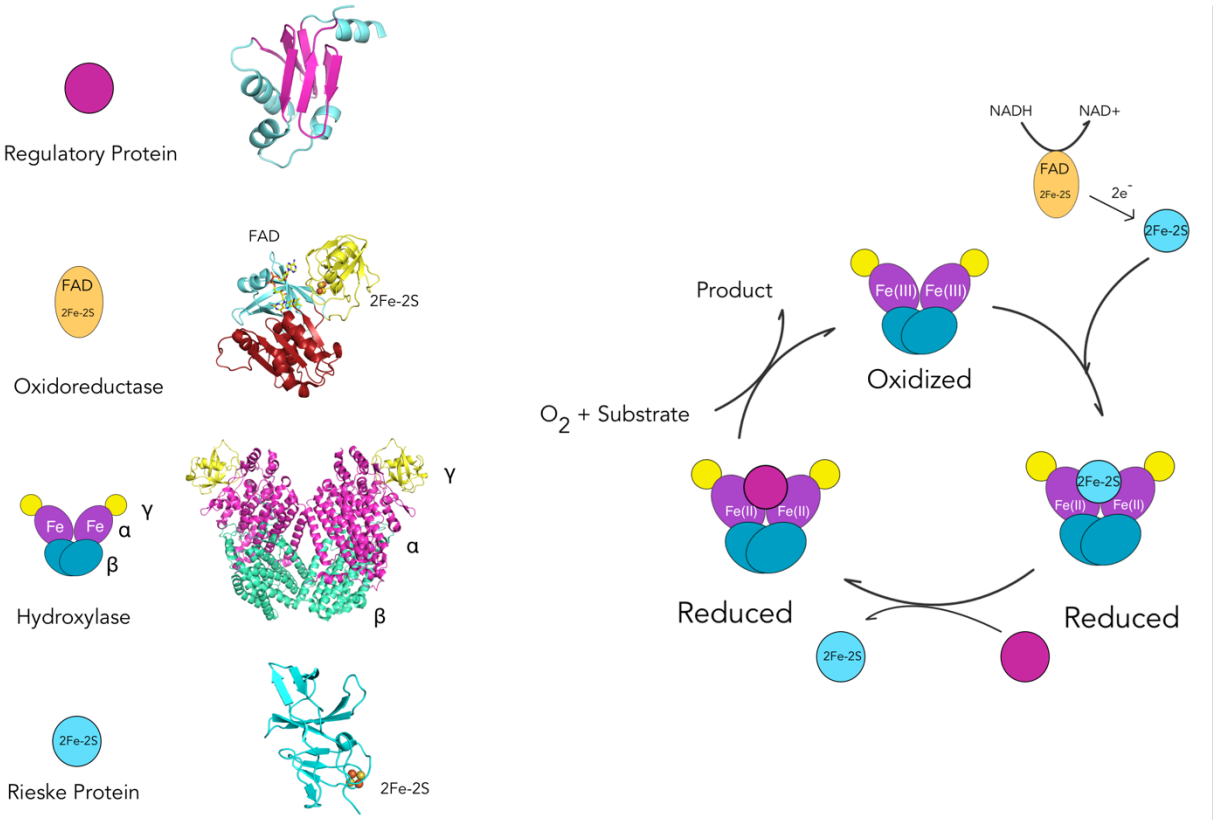

Figure 2: *Representation of the components of TMOs in the context of the catalytic cycle.* Various components of a generalized four component TMO including the regulatory protein (PDB ID: 2BF2), the oxidoreductase (PDB ID: 4WQM), the hydroxylase (PDB: 3DHG) and the rieske protein (PDB ID: 4P1C), are represented with respect to their structure and role in the BMM catalytic cycle. Electrons flow from the electron rich substrate NADH through the reductase and the rieske protein, and reduce the diiron center in the hydroxylase component. Regulatory protein interaction with the hydroxylase then promotes dioxygen activation and hydroxylation of substrate molecules, reverting the hydroxylase to an oxidized state.

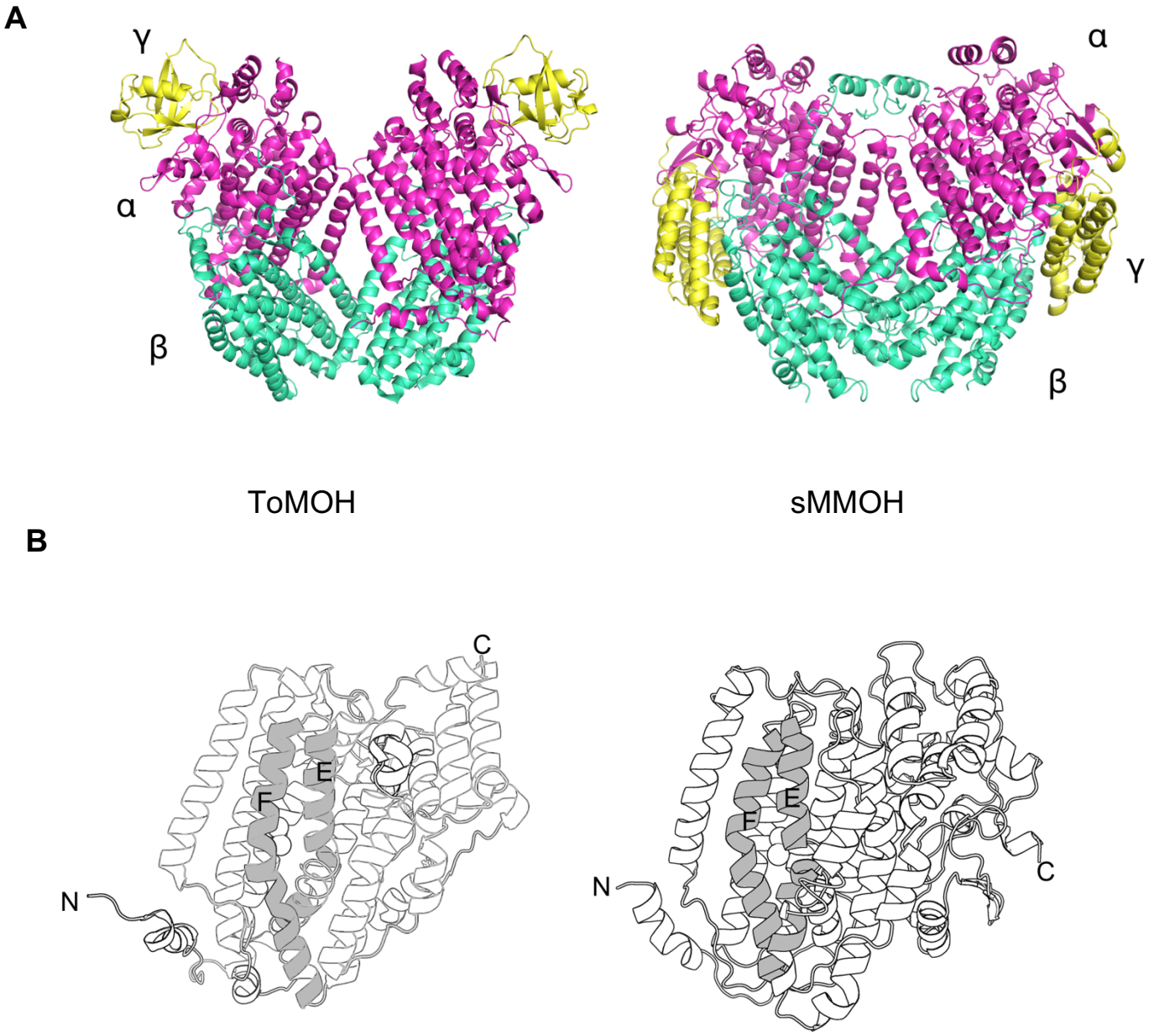

Figure 3: *Structural comparison of the hydroxylase component of ToMO and sMMO***.** ToMO hydroxylase (left) and sMMO hydroxylase (right) are presented as ribbon diagrams. **A)** $\alpha_2\beta_2\gamma_2$ protomer forms of sMMOH and ToMOH. Both proteins display similar global topology with respect to the α (purple) and β (green) subunits but poor sequence homology, especially between γ (yellow) subunits. **B)** The α-subunits of both ToMOH and sMMOH presented as ribbon diagrams. Helices E and F, regions important for hydroxylase interaction with other protein components, are denoted. Each subunit contains two iron atoms assembled within the four-helix bundle involving helices B, C, E and F.

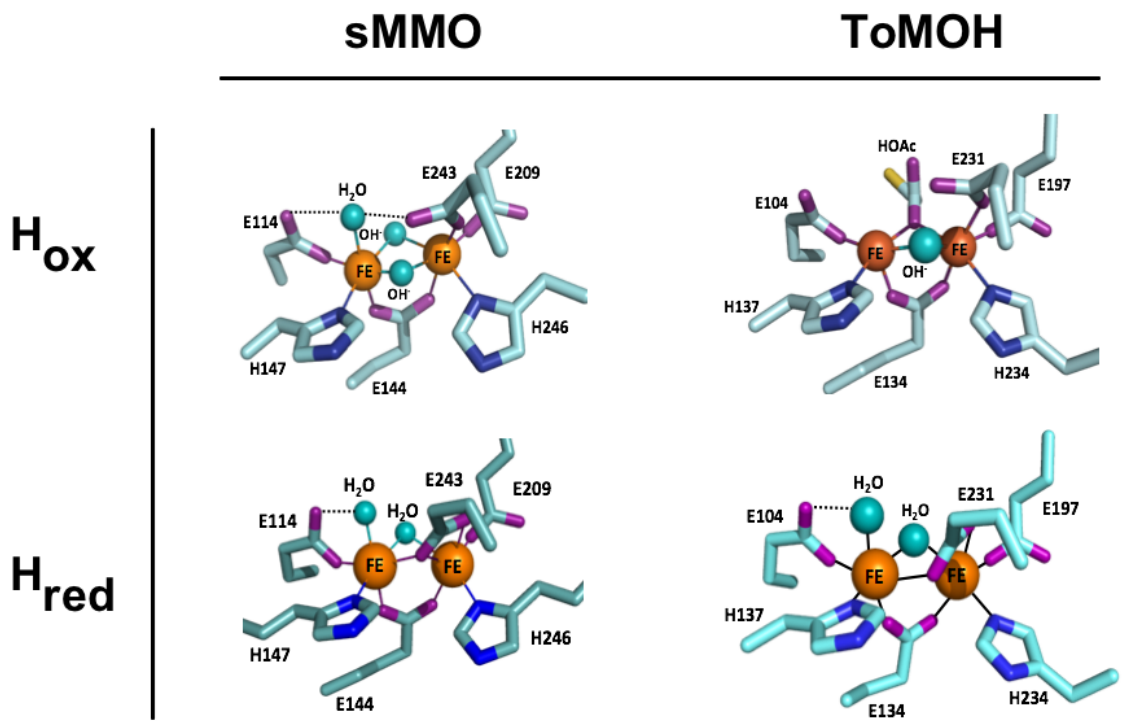

Figure 4: *Comparison of active sites of ToMOH and sMMOH in reduced and oxidized states in the absence of the regulatory protein.* Cursory examination of the active sites of ToMOH and sMMOH indicate a high degree of structural conservation in the resting H_{ox} state. Both sites contain a consistent ligand motif – two histidines, four glutamates, with one glutamate (E144 / E134) acting as a bridging carboxylate. Water molecules or hydroxide ions are also found in bridging positions. Comparison of H_{red} states suggests different core geometries, and hence different ligand field environments around the diiron centers, after center reduction. Figure adapted from (60).

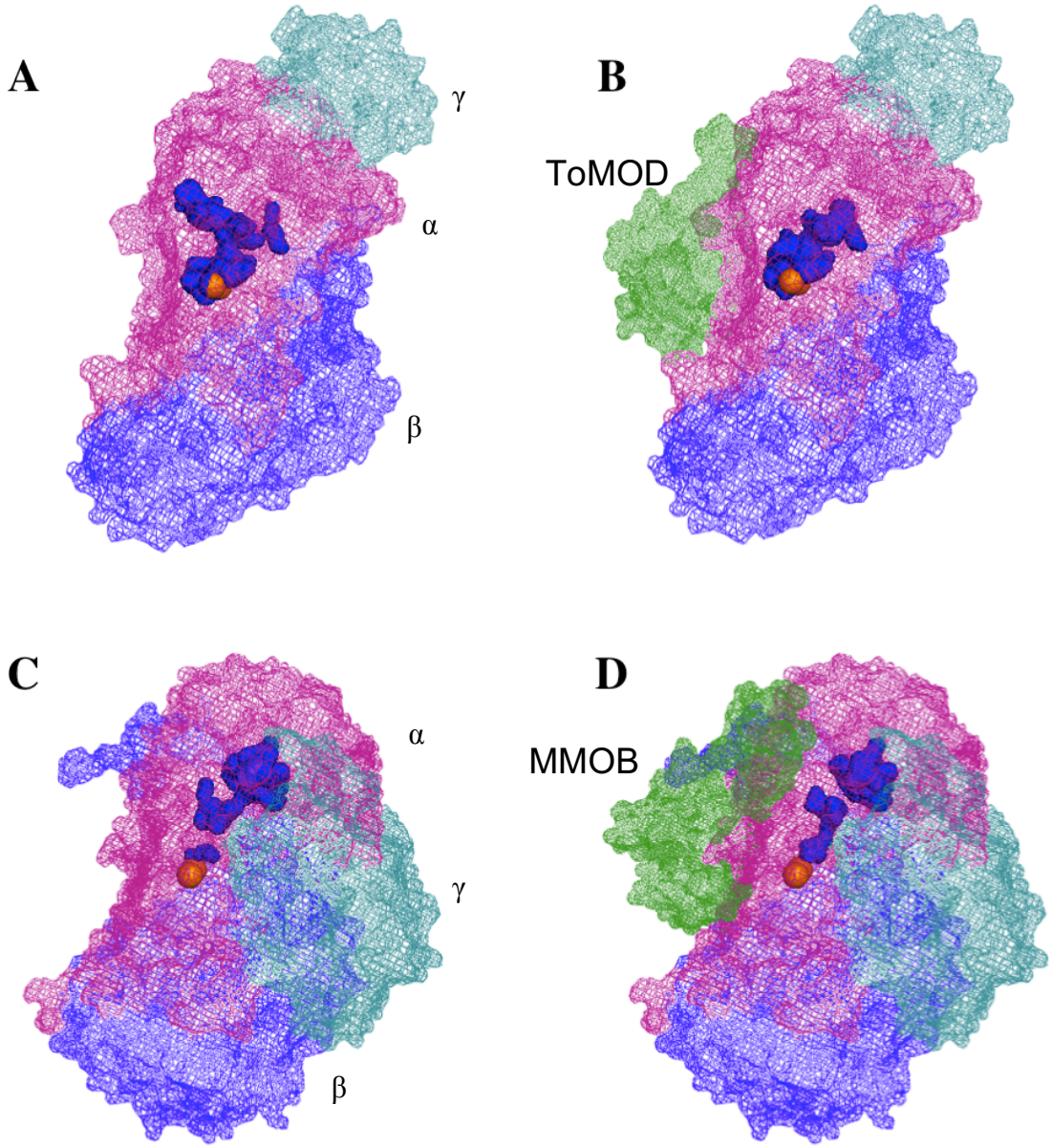

Figure 5: *Effect of regulatory protein binding on the conformations of the substrate access channel in sMMOH and T4MOH*. The α (purple), β (blue) and γ (teal) subunits of T4MOH and sMMOH are depicted before and after regulatory protein binding (green). Pocket or channels spaces are colored as blue surfaces, and iron atoms colored as orange spheres. **A)** $T4MOH_{ox}$ when converted to **B)** $T4MOH_{red}$ bound to T4MOD, the entrance to a contiguous substrate channel appears to close. When **C)** $sMMOH_{ox}$ is converted to **D)** $sMMOH_{ox}$ bound to sMMOB, pockets previously linked in $sMMOH_{ox}$ are observed to disconnect while new connections form. Figure adapted from (62).

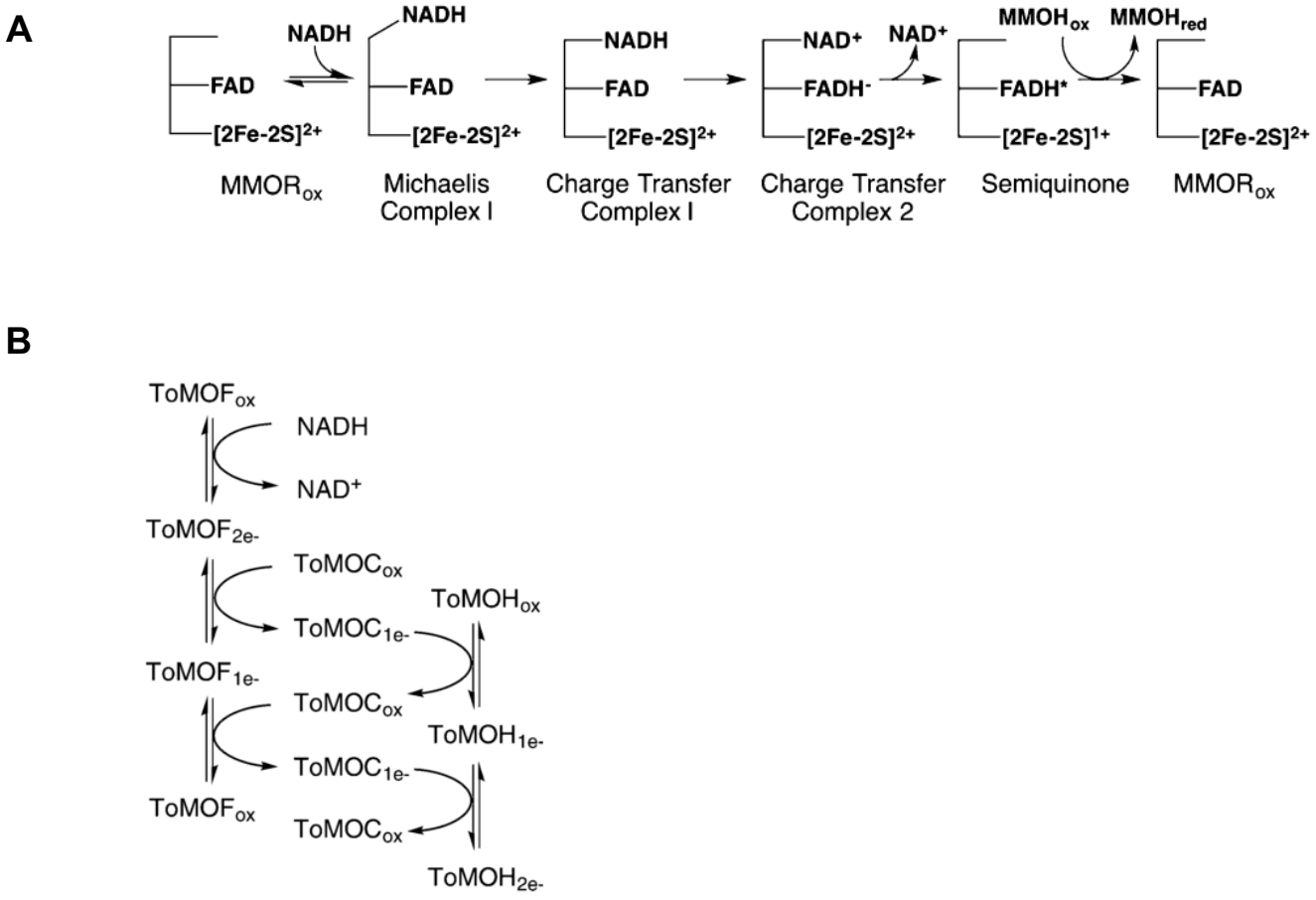

Figure 6: *Models of electron transfer to sMMOH and ToMOH from NADH cofactor*. A further dissection of the electron transfer process on sMMO and ToMO are presented. **A)** sMMOR oxidizes the electron-rich substrate NADH to NAD^+ at an internal FAD domain. The resulting Charge Transfer Complex 2 undergoes internal electron rearrangement to from a semiquinone intermediate with a reduced [2Fe-2S] cluster. This intermediate with distributed charge can then reduce the diiron center of sMMOH via two single electron transfer steps. **B)** Electron transfer in ToMO utilizes a rieske protein ToMOC to shuttle electrons between the reduced ToMOF reductase and the diiron center of ToMOH. ToMOF initially oxidizes NADH in a two-electron transfer step. ToMOC then facilitates two single electron reductions from the reduced [2Fe-2S] cluster and FAD domain to yield the reduced hydroxylase ToMOH.

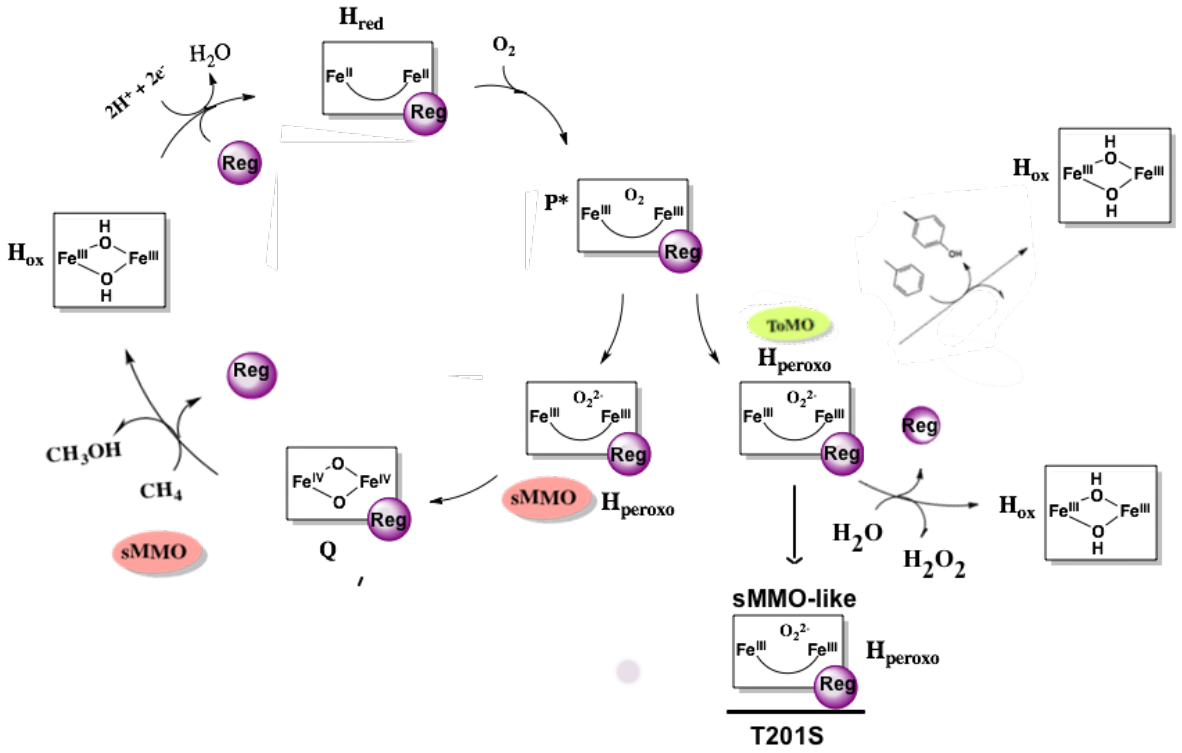

Figure 7: *The catalytic cycle of sMMO and ToMO with respect to relevant intermediates.* Initially, sMMOH and ToMOH in an oxidized H_{ox} state are reduced to form a H_{red} intermediate with the regulatory protein component bound. Both BMMs subsequently activate dioxygen to form a short-lived peroxo-conjugated intermediate P* which rapidly decays to form the H_{peroxo} state, which is a diiron(III) complex. Here, reaction pathways differ. $sMMOH_{peroxo}$ can evolve into a diiron(IV) intermediate with a μ-bis-oxo diamond core geometry, termed Q. The Q intermediate can activate the C-H bond of most alkanes, including methane, leading to substrate conversion into an alcohol. $ToMOH_{peroxo}$ is distinctly different. It may decay in the absence of substrate to H_{ox} by releasing the peroxide conjugate as H_2O_2. Alternatively, it may directly hydroxylate an electron rich aromatic or alkene system to complete the reaction cycle. A T201S mutation has been found to induce the formation of a new H_{peroxo} state that is closer spectroscopically to sMMO. However, this state does not appear to progress to form an intermediate similar to Q in sMMO.

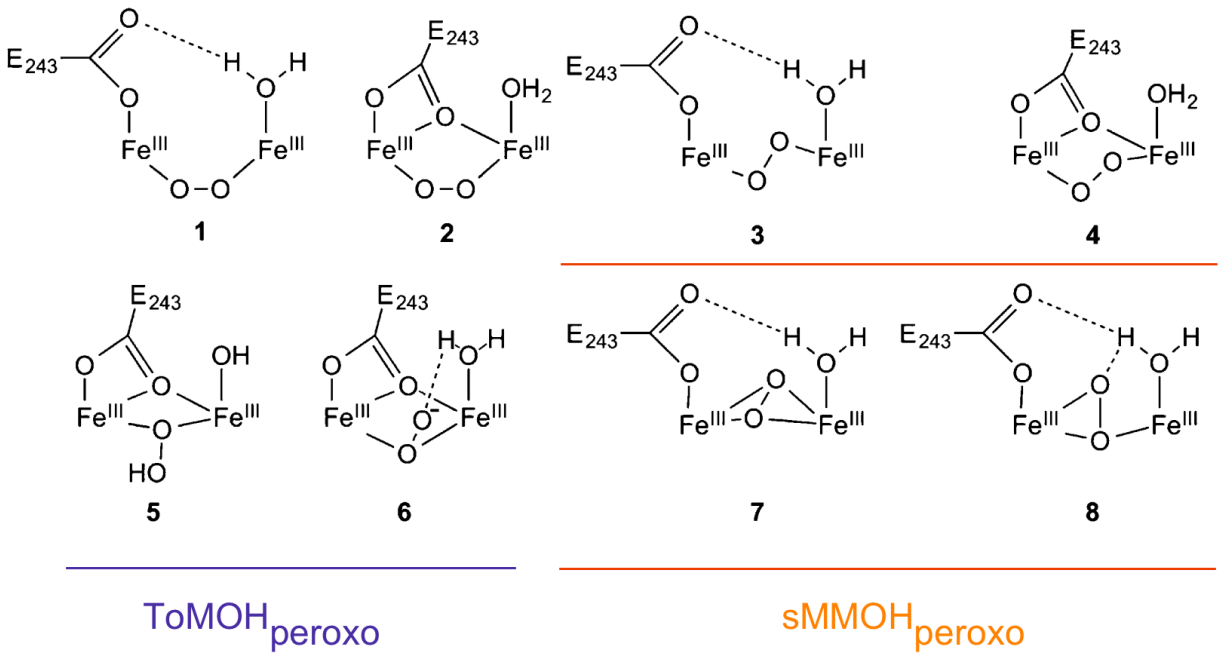

Figure 8: *Proposed models of peroxodiiron(III) core geometry in the H_{peroxo} state*. Mössbauer and optical spectroscopy suggest the ToMOH and sMMOH peroxo intermediates may assume different geometries depending on the position of E243 in sMMOH or E231 in ToMOH. Various models of these intermediates derived from known compounds with well characterized spectroscopic parameters are presented here. Both $sMMOH_{peroxo}$ and $ToMOH_{peroxo}$ are believed to be a μ-1,2-peroxodiiron(III) species. However, the position of the dioxygen ligand is thought to differ between the two. Models 3,4,7,8 with oxygen in a bridging position are thought to best represent $sMMOH_{peroxo}$, while models 5 and 6, with oxygen in an end-on binding position, might represent $ToMOH_{peroxo}$. This difference in intermediates is considered a partial explanation for the lack of formation of intermediate Q in ToMO.

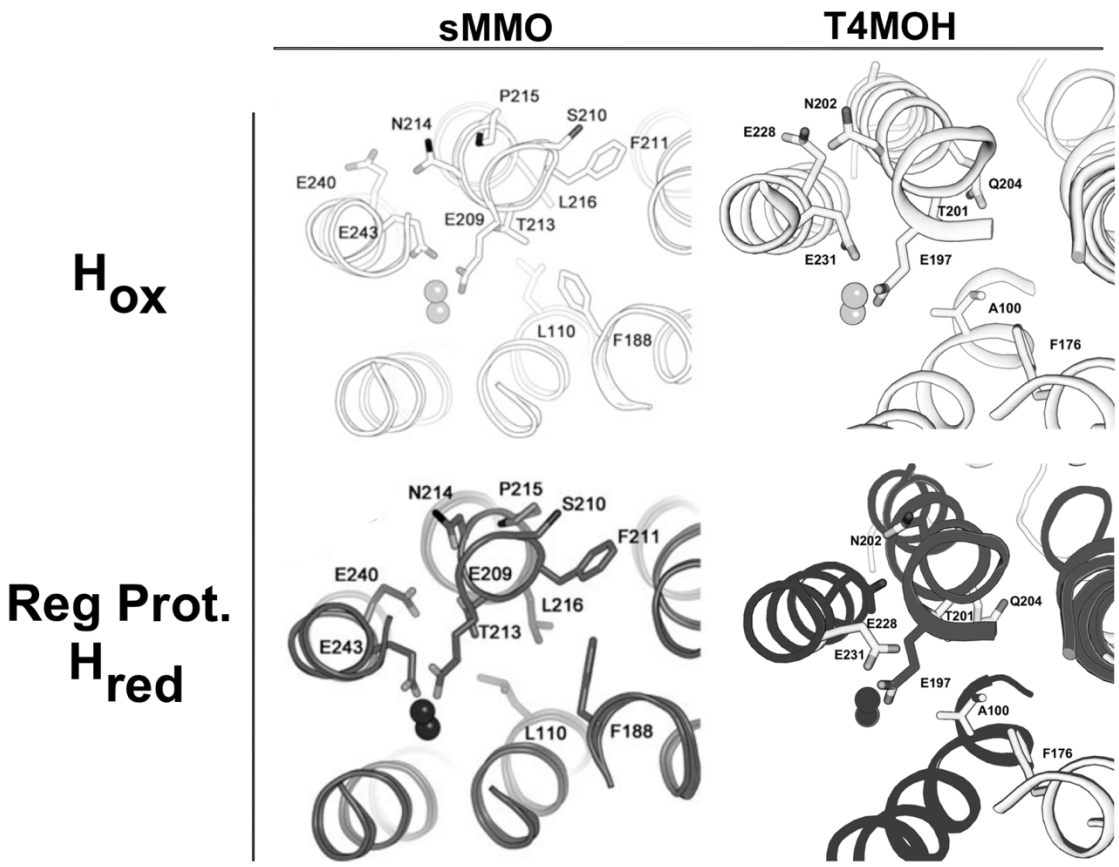

Figure 9*: Changes in active site of the hydroxylase component of sMMO and T4MO upon regulatory protein binding.* A side on view of the four-helix bundle demonstrates how residues directly coordinating the metal center as well as those positioned in helices E and F vary in conformation after sMMOB or T4MOD binding. Key changes include greater displacement of N214 from the interior of helix E in sMMO than for the equivalent residue N202 in T4MO. Also, in both models equivalent residues E240 and E228 rotate towards the metal center as a result of regulatory protein binding. E243 and E231 also display the expected change in coordination geometry. Adapted from (1).

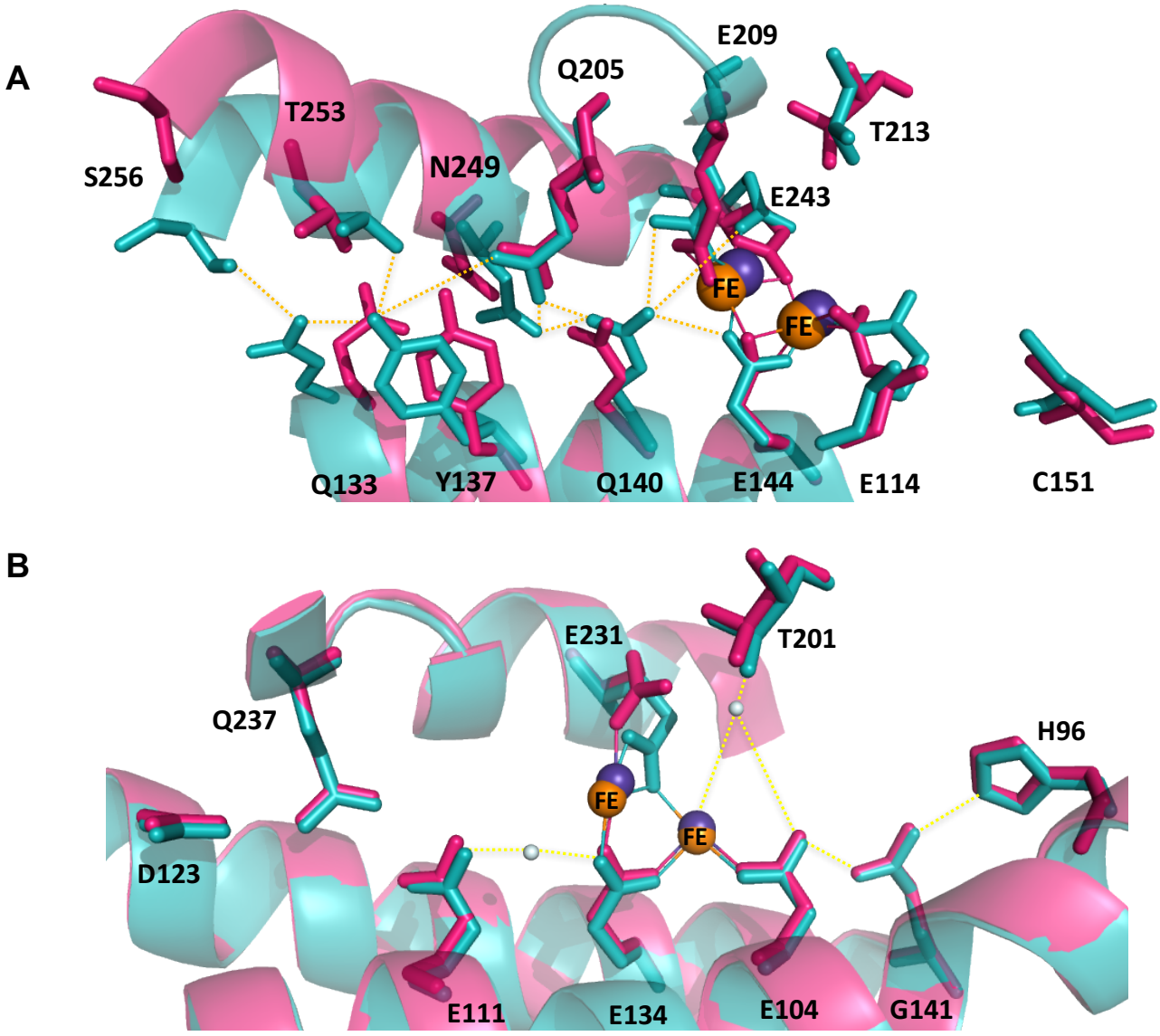

Figure 10: *Structural changes in the hydrogen bonding networks of sMMOH and T4MO after regulatory protein binding*. **A)** In sMMO, key residues participating in the extended hydrogen bonding network are depicted before (blue) and after (pink) sMMOB binding and diiron center reduction. Iron atoms are depicted in orange. Coordinating ligands are found to shift by distances of ~ 1- 2 Å. **B)** Similarly, T4MOH residues within secondary and tertiary hydrogen bonding spheres are shown before (blue) and after (pink) T4MOD binding and diiron center reduction. In contrast to sMMOH, no significant positional changes are observed in coordinating ligands aside from E231, which shifts away a bidentate to monodentate coordination geometry. The diiron center is found to shift less than 1Å. Here, T4MO behavior is considered representative of ToMOH behavior due to a highly (96%) conserved structural arrangement. Figure adapted from (60).

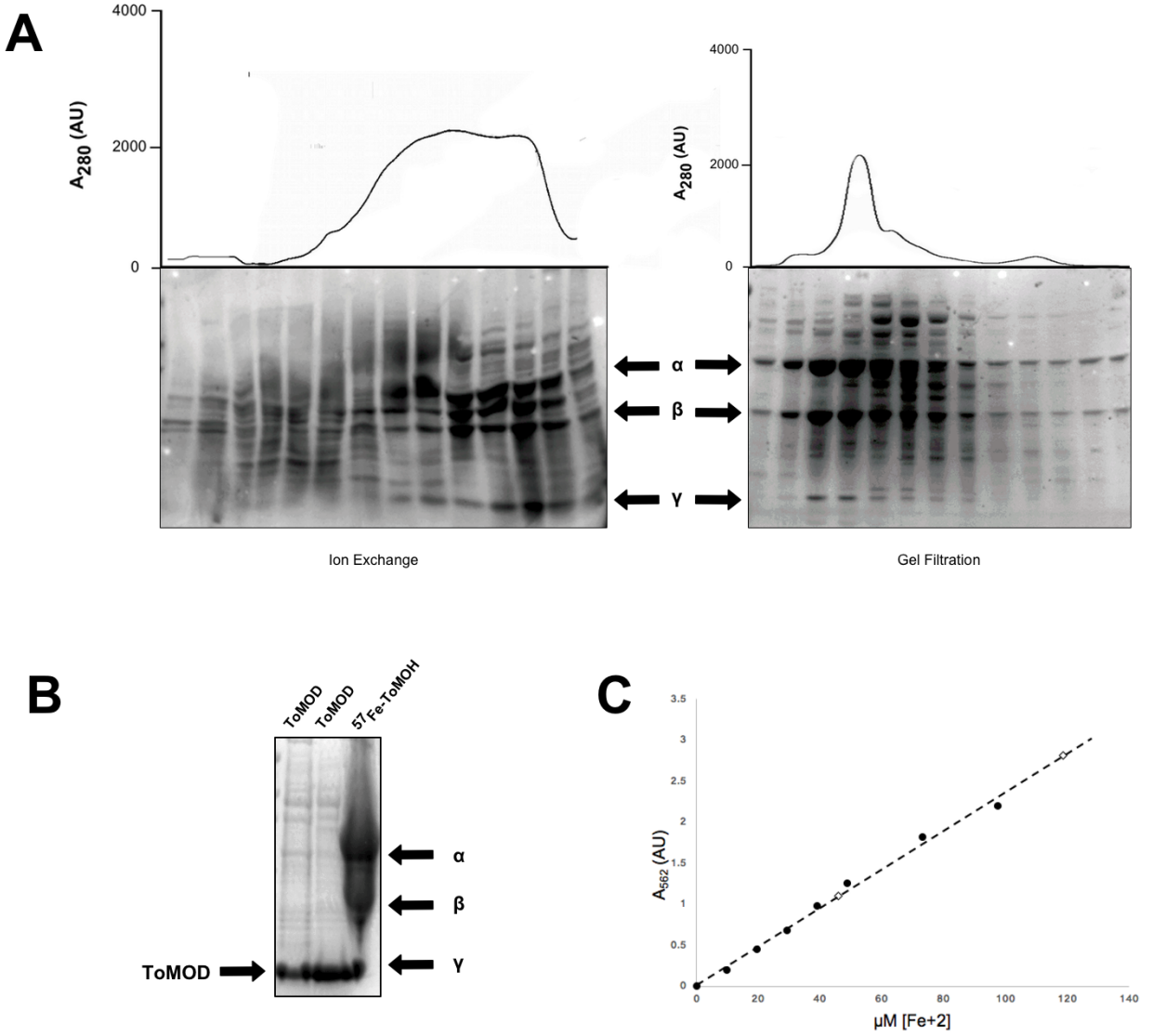

Figure 11: *Purification of ^{57}Fe ToMOH for Nuclear Resonance Vibrational Spectroscopy and Rapid Freeze Quench Mössbauer studies***.** ToMOH was prepared with iron-57 to yield isotopically enriched diiron centers. Sufficient quantities of ToMO regulatory protein ToMOD were also prepared. **A)** Hydroxylase purified via Ion-Affinity chromatography with a Q-Sepharose resin, followed by purification via gel filtration with Sephadex-200 resin. FPLC traces and SDS PAGE analysis of corresponding fractions are presented. **B)** Recombined enriched fractions analyzed via SDS PAGE alongside ToMOD samples to identify impurities. **C)** ToMOH samples (♦) were analyzed by ferrozine assay, and compared to a standard curve (●) generated from known concentrations of Fe^{2+} to determine the approximate concentration of diiron centers. Concentrated ^{57}Fe ToMOH samples were found to have approximately 2.43 mM diiron centers.

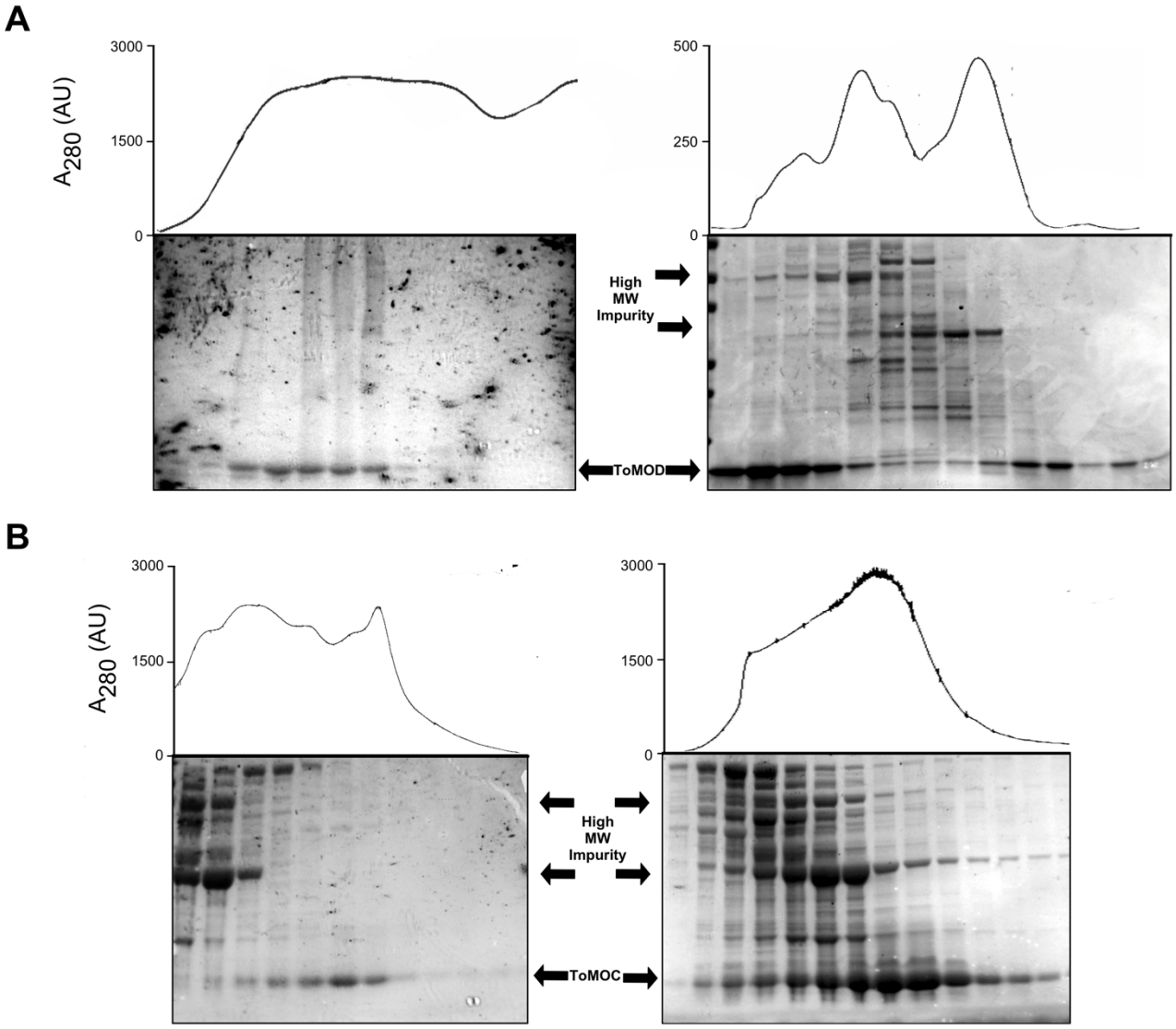

Figure 12: *Batch Expression and Purification of ToMOC and ToMOD***.** ToMO regulatory protein (ToMOD) and rieske protein (ToMOC) were expressed via pET22b+ vectors in BL21(DE3) *E.coli* cells, and subsequently purified. **A)** ToMOD was purified via an improved two-column process using Ion-Affinity chromatography with a Q-Sepharose resin, followed by gel filtration using tandem columns with a Sephadex-200 resin. A representative SDS PAGE analysis of fractions eluted in both steps are presented alongside associated FPLC traces. **B)** A similar purification process was utilized for ToMOC. Ion-Exchange was carried out using a Q-Sepharose resin. Gel filtration was carried out with Sephadex-75 resin. Representative SDS PAGE analyses of both steps are presented alongside their associated FPLC traces.

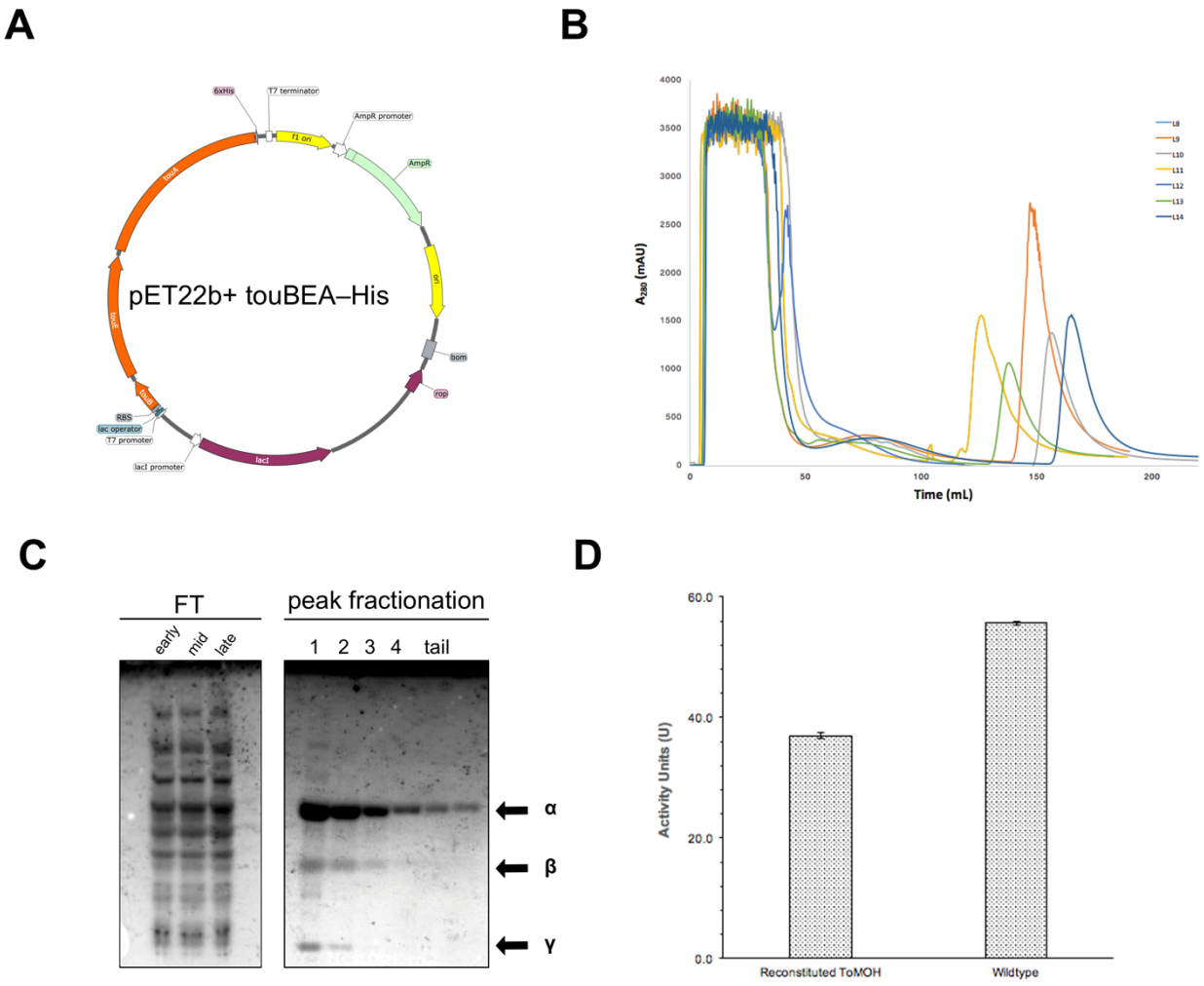

Figure 13: *His-tagging of ToMOH and Purification Optimization.* **A)** Sequencing of the pET22b+ vector containing the recombinant ToMOH gene revealed a potential linker between the α-subunit of the hydroxylase's C-terminus and a 6X his-tag. Site directed mutagenesis was carried out to remove a stop codon preventing terminus-tag fusion by a third party (Genewiz). **B)** ToMOH was purified via IMAC. Buffer optimization was carried out to improve yield. Sample FPLC traces associated with trial buffers are presented as an indicator of successful optimization. **C)** Both flow-through and purified fractions were analyzed via SDS PAGE to determine purity of eluted fractions, and degree of recovery. A sample SDS PAGE analysis is presented. Impurities normally present in the standard two-column purification are absent in eluted fractions. **D)** Aromatic hydroxylation activity of reconstituted his-tagged ToMOH was determined in comparison to wildtype. Activity is approximately 64% of wildtype.

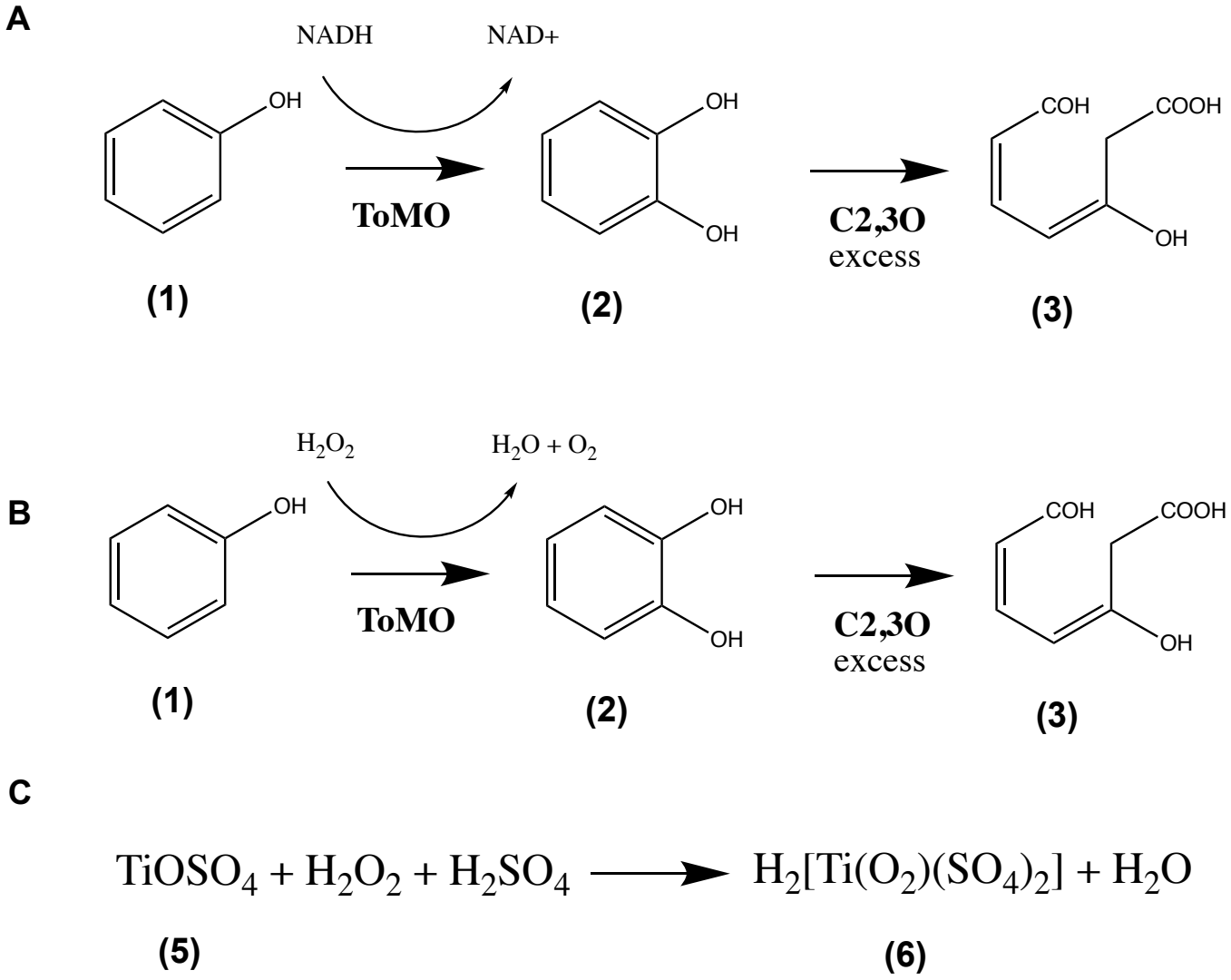

C

$$TiOSO_4 + H_2O_2 + H_2SO_4 \longrightarrow H_2[Ti(O_2)(SO_4)_2] + H_2O$$

(5) (6)

Figure 14: *Activity assays for characterizing ToMO Variants*. A variety of activity assays are utilized in this work. **A)** Aromatic hydroxylase activity can be determined by examining the conversion of (1) phenol to (2) catechol by ToMO, and the subsequent rapid conversion of catechol to 2-hydroxymuconic semialdehyde (ε_{410nm} = 12620 M^{-1} cm^{-1}) by C2,3O. NADH is provided as an electron rich substrate to initiate the reaction. **B)** Peroxidase activity can be determined by examining the same conversion as when assaying for aromatic hydroxylation, with the use of peroxide as a substrate rather than NADH. **C)** Levels of peroxide in solution can be quantified by reacting peroxide with (5) $TiOSO_4$ detection reagent acidified in sulfuric acid. The peroxide and reagent can react to form a (6) perititanic acid complex which absorbs strongly at 407 nm, and is detectable by UV-Vis spectroscopy.

A

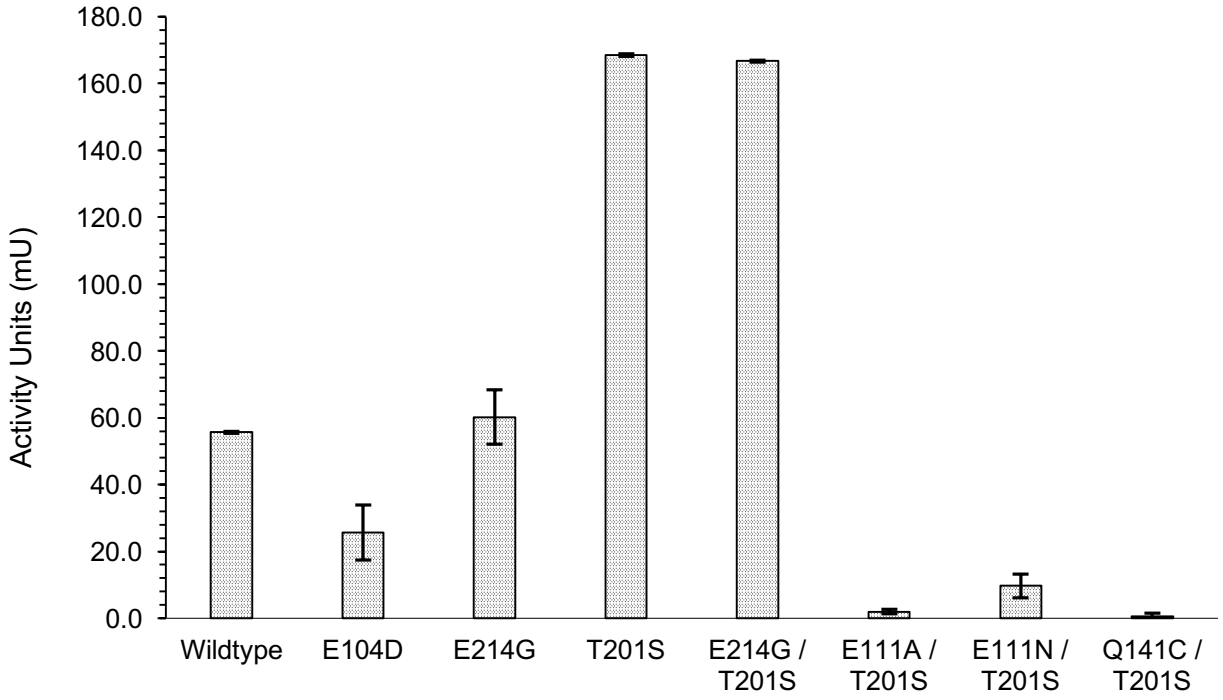

B

Mutant	Catechol Oxidase Activity (mU)	NADH Coupling Ratio**
Wildtype	55.7 ± 0.3	0.38
E104D	25.6 ± 8.3	0.75
E214G	60.2 ± 8.1	0.15
T201S	168.5 ± 0.5	0.27
E214G / T201S	166.7 ± 0.3	0.20
E111A / T201S	2.0 ± 0.6	0.13
E111N / T201S	9.7 ± 3.6	0.08
Q141C / T201S	0.5 ± 1	0.00

Figure 15: *Aromatic Hydroxylation activity of wild-type ToMO and ToMO variants*. **A)** Various relevant ToMO variants were assayed for their ability to convert phenol to catechol, and activities (mU) are presented. **B)** Calculated activities in the conversion of phenol to catechol for various ToMO variants is presented alongside estimated NADH coupling ratios. NADH coupling data was obtained from (62). Relevant experimental parameters are presented in Table 4.

A

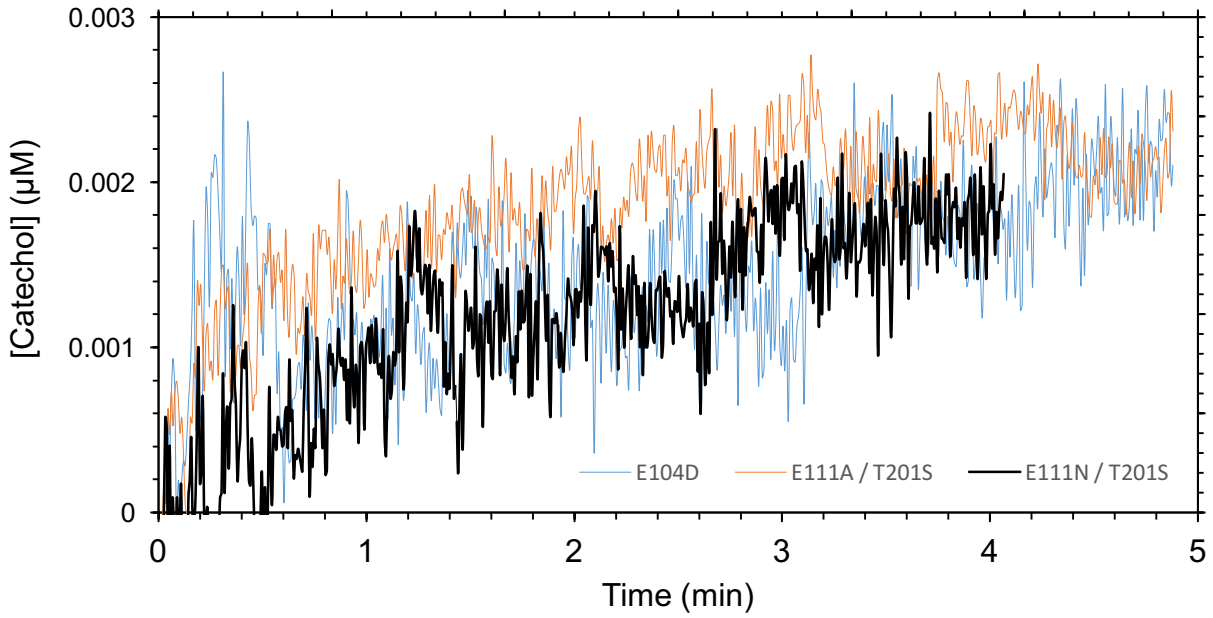

B

Mutant	Peroxidase Catechol Activity (mU)	Superoxide Activity
E104D	0.005 ± 0.1	~ 0
E111A / T201S	0.003 ± 0.2	~ 0
E111N / T201S	0.003 ± 0.2	~ 0

Figure 16: *Peroxidase Activity of ToMO Variants*. ToMOH variants E104D, E111A / T201S and E111N / T201S were assayed for their ability to utilize peroxide as a substrate in the conversion of phenol to catechol. **A)** Sample Time-course activity measurements for ToMOH variants assayed. Each trace, E104D (–), E111A/T201S (–), E111N/T201S (–) demonstrates significant noise, and a minimal change in activity. **B)** Calculated rates of peroxidase activity in the conversion of phenol to catechol and superoxide activity for relevant TOMOH mutants. Initial rates were determined by linear approximation in the initial phase of the time-course kinetic data. Of note, error rates suggest peroxidase activity is negligible in all variants assayed.

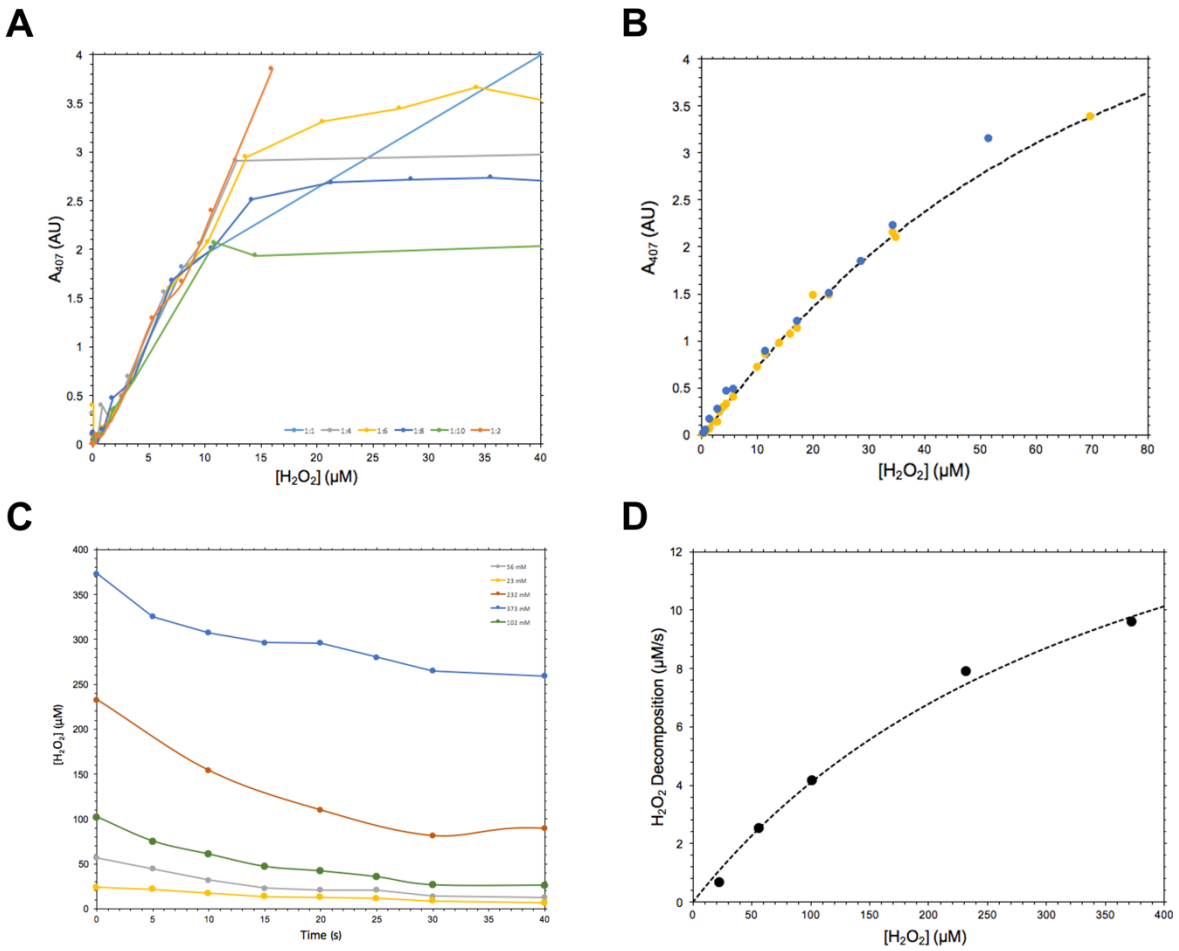

Figure 17: *Development and Validation of a Catalase and Peroxidase Quantification Assay*. A colorimetric assay utilizing acidified $TiOSO_4$ was developed to determine whether various ToMOH variants were capable of consuming or producing H_2O_2. The resulting complex formed by H_2O_2 and $TiOSO_4$ absorbs strongly at 407 nm. **A)** Various solutions of acidified $TiOSO_4$ detection reagent were reacted with H_2O_2 samples of known concentration to determine a combination ratio yielding a linear response with good sensitivity. **B)** Standard curves utilizing a known quantity of H_2O_2 were constructed to determine assay reproducibility and establish minimum and maximum quantifiable limits. Two examples curves, (● and ●) were not found to deviate significantly. Nonlinear fitting of experimental data yielded the relationship $A = 5.04\text{-}5.06EXP(\text{-}0.016C)$, with an RMSD < 0.008. **C**) The kinetics of bovine liver catalase mediated decomposition of H_2O_2 at varying concentrations were examined discontinuously at pH 7.5 in phosphate buffer. Initial rates were extrapolated from the first ten seconds of each substrate vs. time curve. **D)** Initial rate of H_2O_2 decomposition for bovine liver catalase was plotted versus substrate concentration and nonlinearly fit to a Michaelis-Menten model.

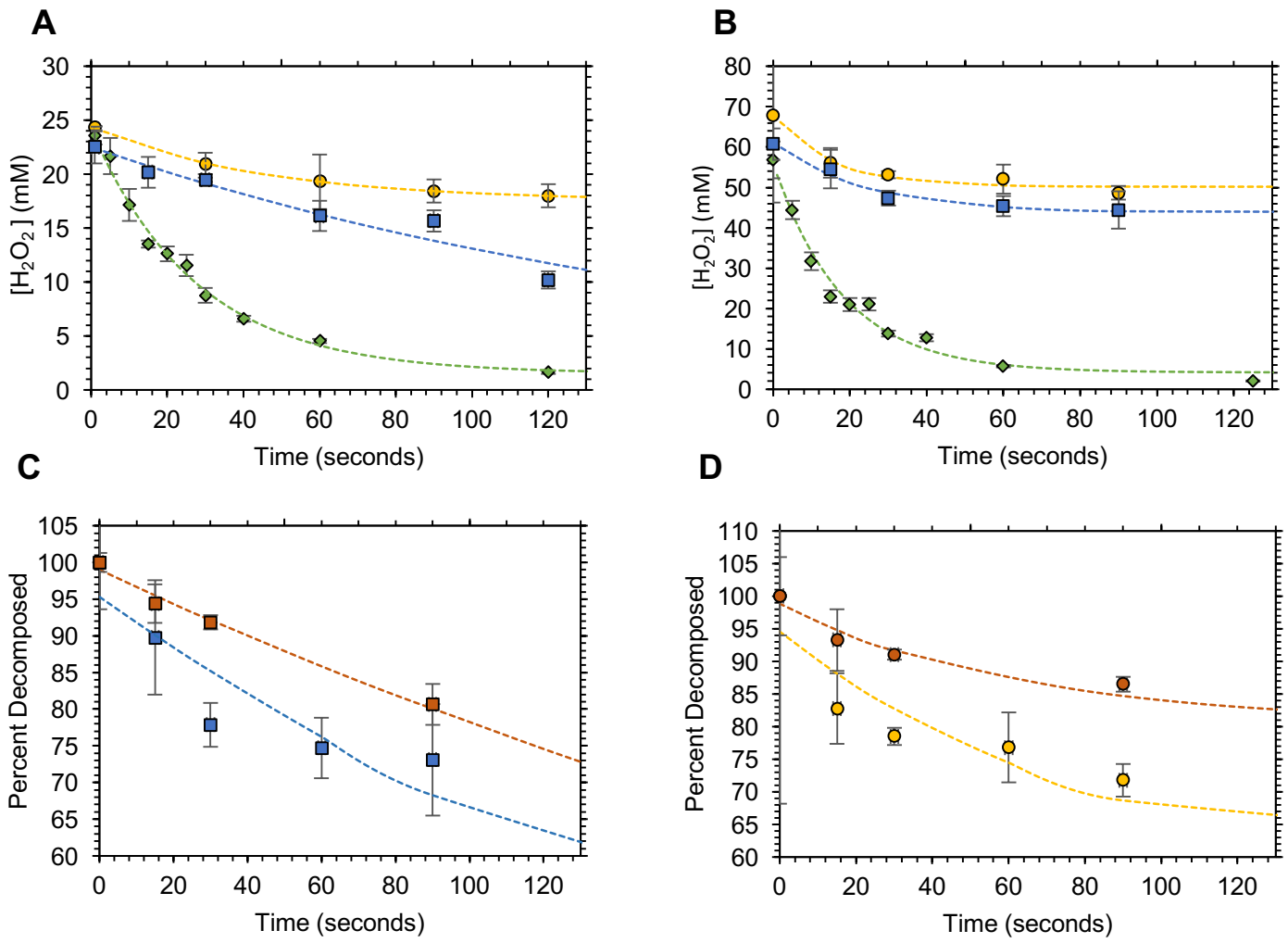

E

Mutant	Initial Rate (µM/s/nmol protein)		
	25 mM H_2O_2	50 mM H_2O_2	50 mM H_2O_2 + 2µM ToMOD
Wild-type	1.3 ± 0.1	9.4±0.8	1.6 ± 0.1
E111A / T201S	1.1 ± 0.1	6.0 ± 0.3	1.0 ± 0.1
Catalase	113 ± 9	396 ± 31	N/A

Figure 18: *Kinetics of the decomposition of H_2O_2 by ToMOH variants and bovine liver catalase*. Wild-type ToMOH (●) and mutant E111A / T201S ToMOH (■) and bovine liver catalase (♦) were assayed for their ability to decompose peroxide in solution, in the absence of other protein components at **A)** 25mM hydrogen peroxide and **B)** 50mM hydrogen peroxide. Time-course kinetic data obtained in triplicate was fit via nonlinear least squares regression, and the initial rate determined per nanomole of protein present. The rate of H_2O_2 decomposition was then examined in the presence of the regulatory protein ToMOD. Collected data for **C)** E111A / T201S ToMOH +D (■) and **D)** wild-type ToMOH + D (●) were compared to D-free treatments after normalization to the initial concentration of hydrogen peroxide present in solution. Kinetic data was fit via nonlinear least squares regression, and the initial rate determined per nanomole of protein present. **E)** Initial rate data obtained from nonlinear least square regression is presented for all protein conditions examined, for various treatments of hydrogen peroxide and ToMOD.

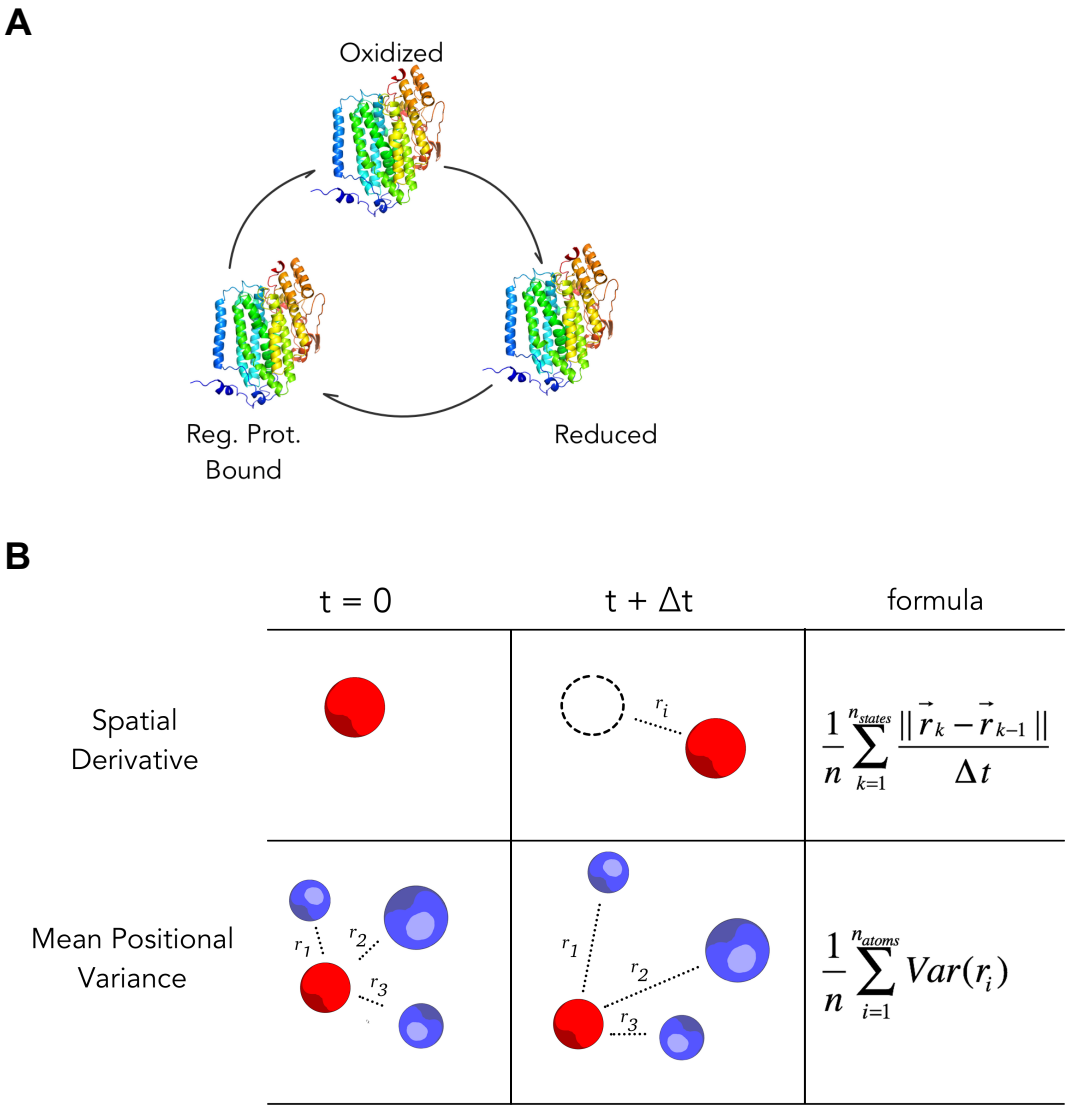

Figure 19: *Graphical depiction of computational methods for assessing protein rigidity.* **A)** Crystal structures of a given protein in various states are obtained, and intermediary structures are simulated through linear interpolation between crystal structures in the order they appear in the catalytic cycle. The relevant states considered for T4MO and sMMO are an oxidized state, a reduced state, and a reduced state with the regulatory protein bound. **B)** Diagrams of two different metrics for calculating the mobility of an atom in a protein bulk over a catalytic cycle are presented. The spatial derivative measures the movement of an atom over given time step Δt, while the mean positional variance measures the changes in interatomic distances between a given atom and all other atoms in the protein bulk over every Δt. In both cases, these metrics are averaged over all atoms within a given residue, or region considered.

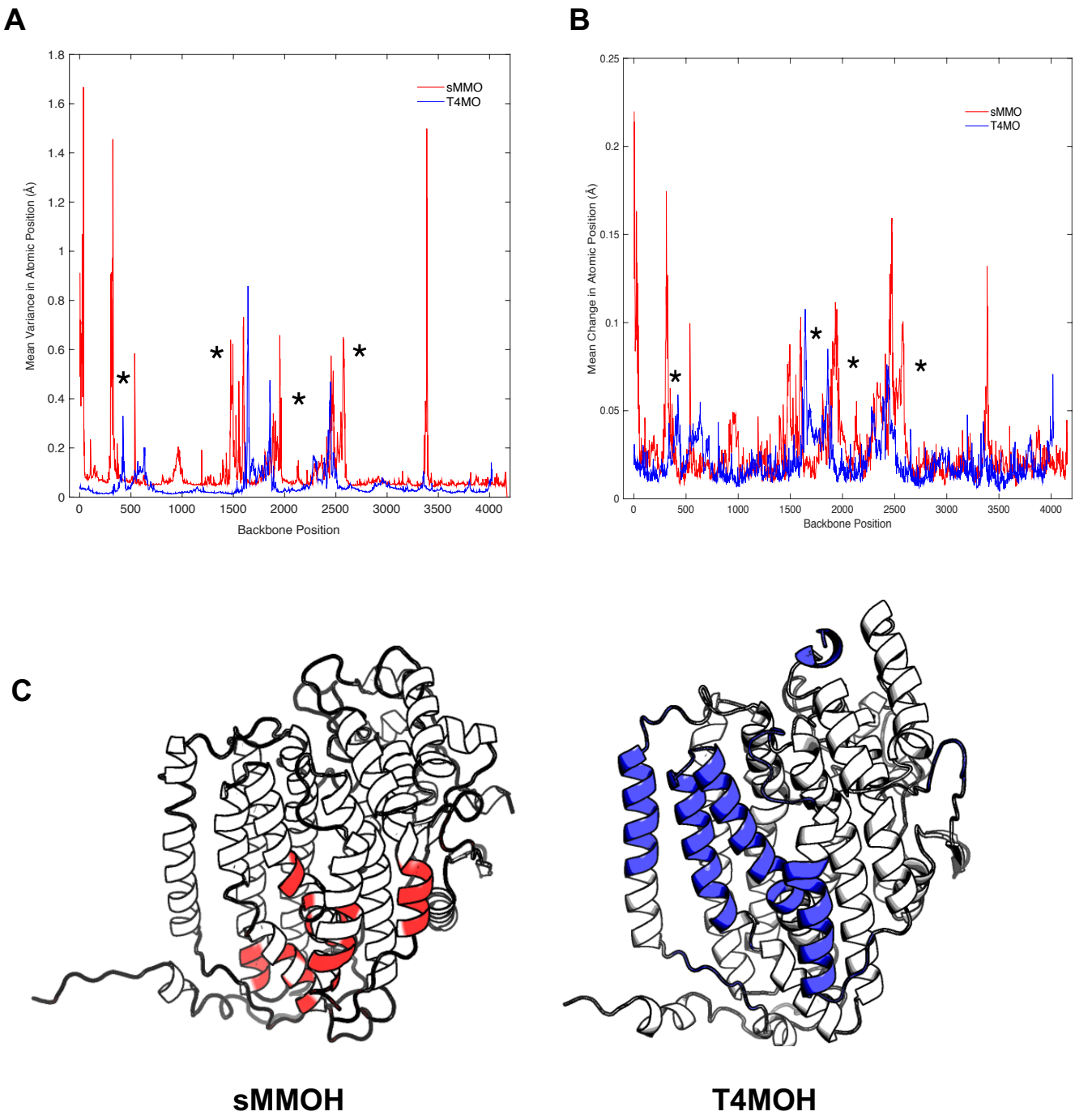

Figure 20: *Analysis of backbone rigidity of sMMOH and T4MOH*. **A)** Mean variance in atomic position, or mean positional variance, over the catalytic cycle was calculated for carbon and nitrogen atoms in the backbones of the α-subunit of sMMOH (red) and T4MOH (blue). **B)** The mean change in atomic position, or the mean spatial derivative, for the same atoms was also determined. Asterisks denote conserved features of high mobility present in each comparison. **C)** Visualization of regions of high mobility in the α-subunit of sMMO and T4MO, determined by identifying the 20% most mobile atoms in each structure.

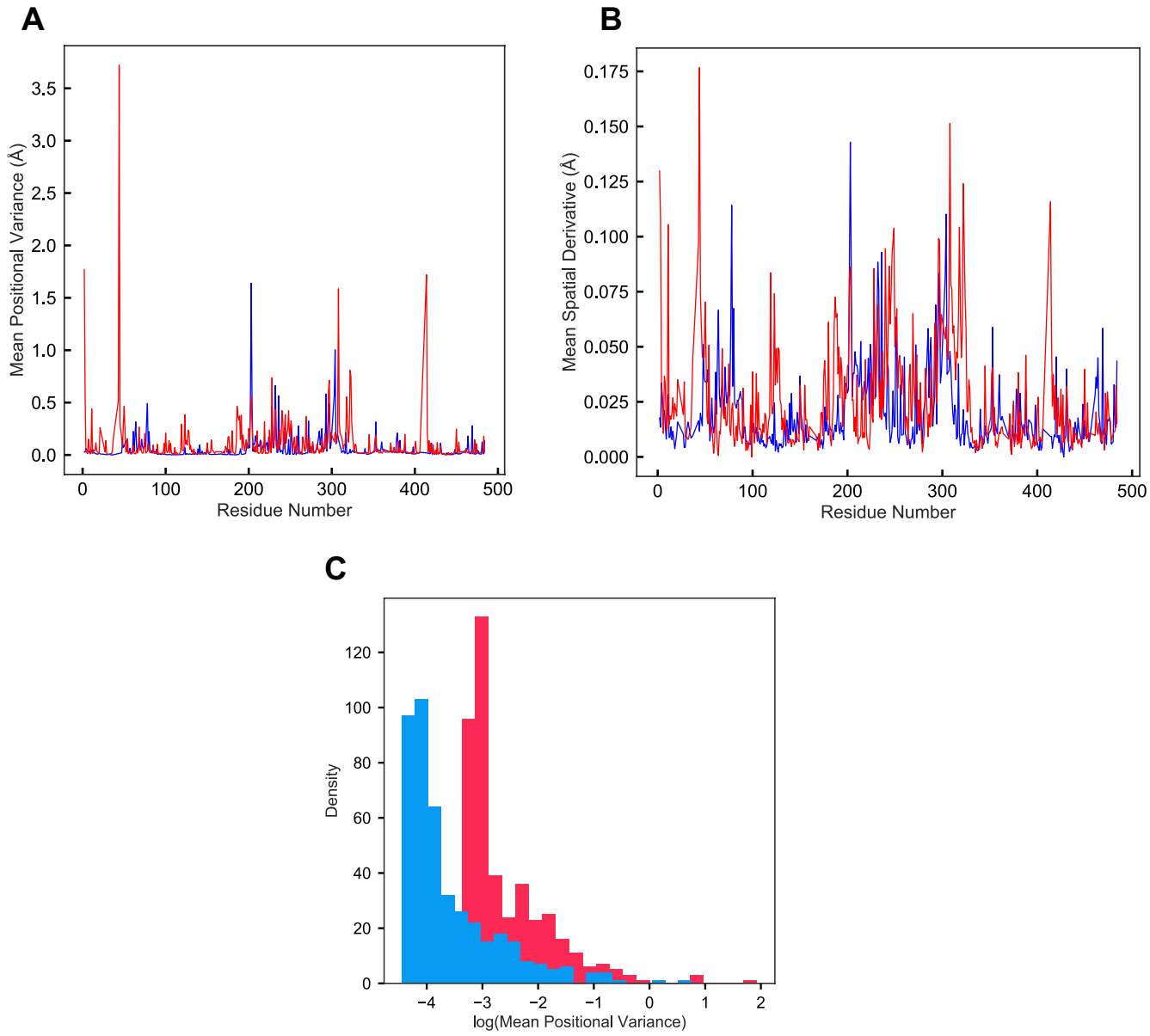

Figure 21: *Analysis of rigidity for structurally similar residues in T4MOH and sMMOH*. For similar residues, defined as those which share < 5 Å difference in position between sMMOH (red) and T4MOH (blue), two metrics for measuring residue mobility were calculated. **A)** The mean positional variance and **B)** mean spatial derivative were determined for 492 paired residues. Residue numbers reflect numbering in T4MO / ToMO. **C)** The distribution of the log base two of mean positional variance in sMMOH and T4MO for equivalent residues demonstrates clear peaks, approximately 2^{-3} Å for sMMO and 2^{-4} Å for T4MO.

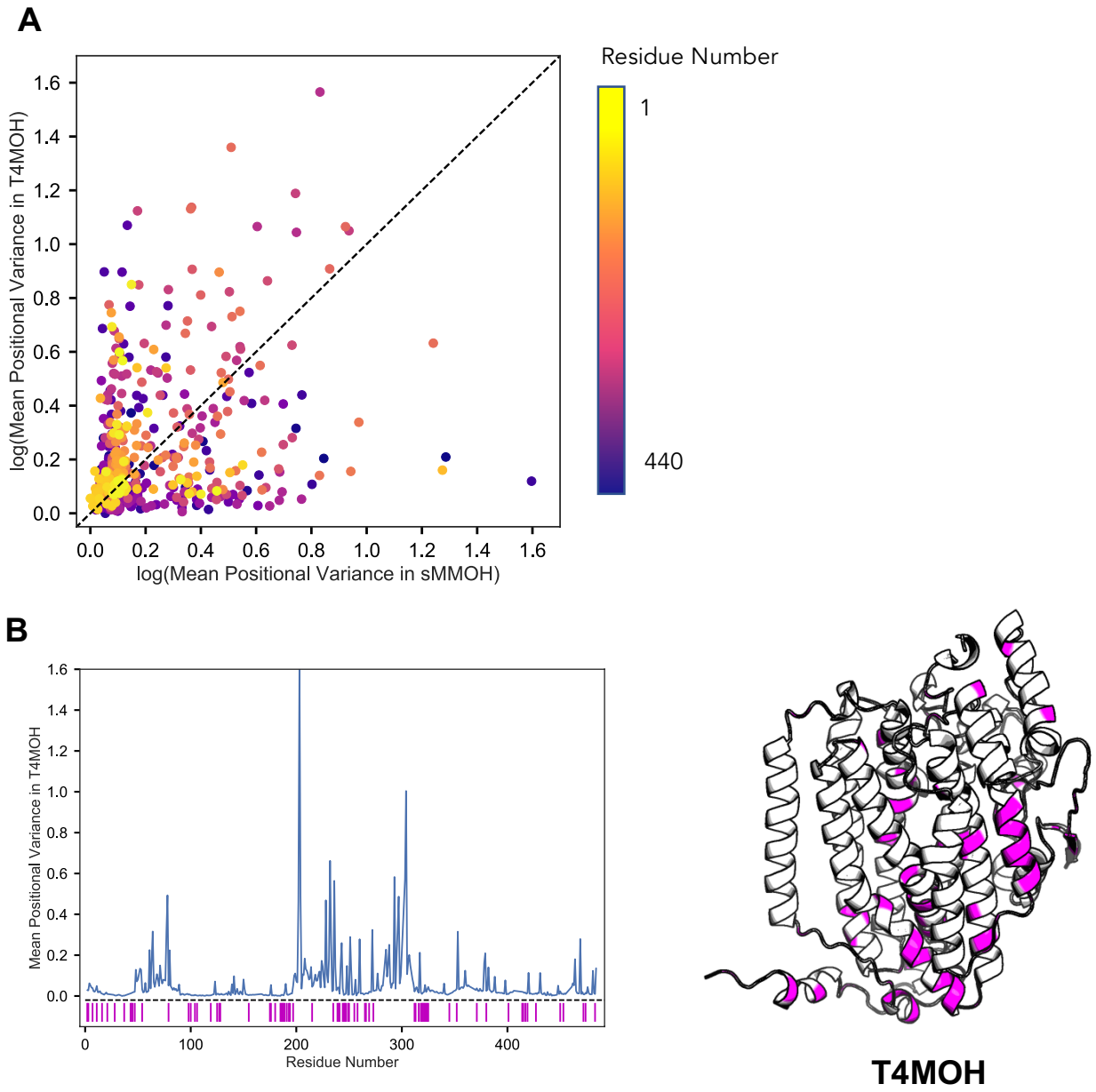

Figure 22: *Identification of differentially mobile residues in T4MOH versus sMMOH*. **A)** For all 492 structurally similar residues, the relationship between the logarithm of the mean positional variance in T4MOH versus sMMOH is examined. Residues with equivalent motion in T4MOH and sMMOH are in proximity to the trend line, indicating a 1:1 relationship. Broadly, residues which appear highly mobile in sMMOH are not mobile in T4MOH, and vice versa. **B)** Residues which displayed lower than average mobility in T4MOH but higher than average mobility in sMMOH are indicated by bar-plot (|) over the mean positional variance in T4MOH (–). Residues matching this criterion are also demonstrated on the α-subunit of T4MOH. Multiple residues are present within the interior of the four-helix bundle. The twenty-five most differentially mobile residues in this category, as determined by the logarithm of the fold change in motion, are presented in Table 8.

A

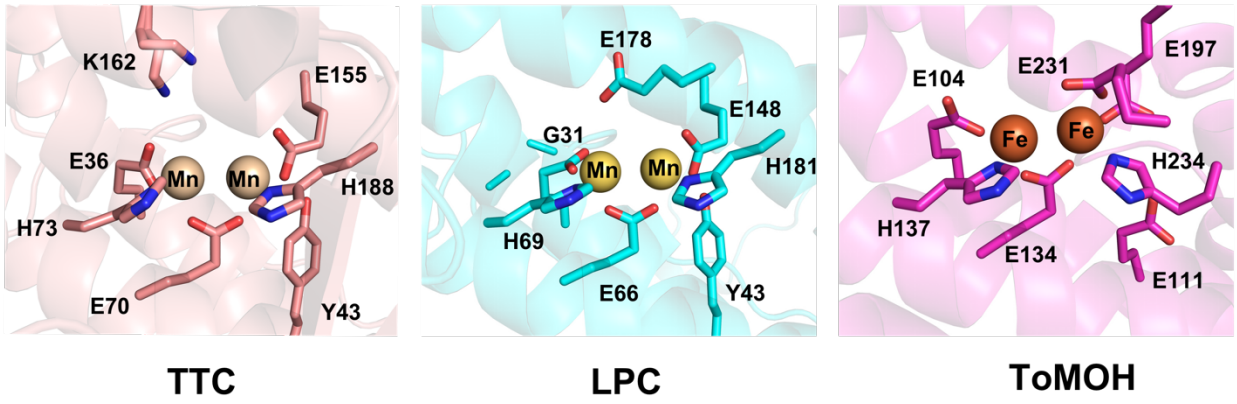

B

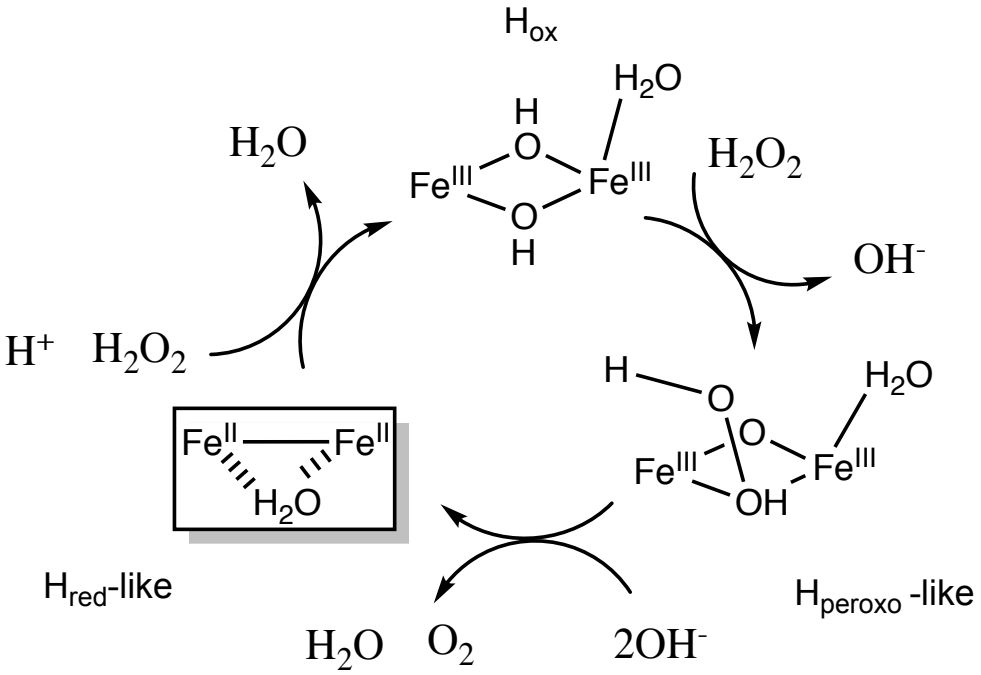

Figure 23: *Comparison of active site pockets of manganese catalases TTC, LPC and ToMOH*. **A)** TTC (PDB ID: 1JKU) and LPC (PDB ID: 2V8U) are binuclear nonheme manganese catalases found in *Thermus thermophiles* and *Lactobacillus plantarum* respectively. Both proteins are members of the ferritin-like superfamily, with a characteristic metal center within a four-helix bundle. Comparison of the active sites to ToMOH (PDB ID: 1TOQ) indicates similar conserved residues and high similarity in residue organization. **B)** A proposed mechanism for ToMOH mediated H_2O_2 degradation derived from the known catalytic cycle of nonheme dimanganese catalases. A diiron(III) species, posited to be the $ToMOH_{ox}$, is thought to bind H_2O_2 by displacing a labile bridging hydroxide ligand, forming an H_{peroxo}-like species. One potential structure for H_{peroxo} is presented here. Subsequent oxidation of H_2O_2 yields a diiron(II) intermediate of unknown structure, thought to resemble H_{red}. Reduction of another H_2O_2 molecule by this species, following a proton transfer step, reverts the diiron center to the oxidized state and completes the reaction cycle.

XI. Tables

Table 1: Trial Buffers Utilized in Optimizing Purification of His-tagged ToMOH

	Buffer	pH	Salt (mM)	Imidazole (mM)	Glycerol	Additives
L1	Tris 50 mM	8	200	20	5% v/v	
L2	Tris 50 mM	8.4	200	20	5% v/v	
L3	Tris 50 mM	8.4	200	0	5% v/v	
L4	Phosphate 20 mM	7.2	200	0	5% v/v	
L5	Phosphate 20 mM	7.6	200	0	5% v/v	N/A
L6	Phosphate 20 mM	7.4	200	20	5% v/v	
L7	Phosphate 20 mM	7.2	200	0	5% v/v	
L8	Phosphate 20 mM	7.2	50	0	5% v/v	
L9	Phosphate 20 mM	7.2	200	10	5% v/v	
L10	Phosphate 20mM	7.0	200	0	5% v/v	
L11	Phosphate 20mM	6.8	200	10	5% v/v	
L12	Phosphate 20mM	7.2	500	0	5% v/v	
L13	MOPS 25 mM	7.0	50	0	0% v/v	
L14	Phosphate 20mM	6.8	200	10	5% v/v	2 mM cysteine 200 μM $Fe(NH_4)_2(SO_4)_2 \cdot 6H_2O$ 8 mM thioglycolate
L15	Phosphate 20mM	7.2	500	0	5% v/v	2 mM cysteine 200 μM $Fe(NH_4)_2(SO_4)_2 \cdot 6H_2O$ 8 mM thioglycolate
L16	MOPS 25 mM	7.0	50	0	0% v/v	2 mM cysteine 200 μM $Fe(NH_4)_2(SO_4)_2 \cdot 6H_2O$ 8 mM thioglycolate

Table 2: Experimental Parameters Utilized in Assaying for Aromatic Hydroxylase Activity

Reactant	[Reactant]
NADH	1 mM
C2,3O	100 μM
H	0.15 μM
C	4 mM
D	10 μM
F	0.30 μM
Phenol	1 mM

Table 3: Experimental Parameters Utilized in Assaying for Peroxidase Activity

Reactant	[Reactant]
NADH	1 mM
C2,3O	100 μM
H	0.15 μM
C	4 μM
D	10 μM
F	0.30 μM
H_2O_2	0.8, 1, 2 mM

Table 4: Experimental Parameters Utilized in Assaying for NADH coupling

Reactant	[Reactant]
NADH	200 μM
H	1 μM
C	2 μM
D	2 μM
F	0.2 μM
Phenol	1 mM

Table 5: Experimental Parameters Utilized in Assaying for H_2O_2 Decomposition Activity

Protein	[Protein]
Wt. ToMOH	1 μM
E111A	1 μM
Catalase	0.06 μM
ToMOD	2 μM

Table 6: Optical UV-Vis and Mössbauer Spectroscopic Parameters of the H_{peroxo} state in sMMO and ToMO Variants

	Optical UV-Vis		Mössbauer	
Variant	λ_{max} (nm)	ε (M^{-1} cm^{-1})	δ (mm s^{-1})	ΔE_Q (mm s^{-1})
MMOH H_{peroxo} (Mt)	725	2500	0.67	1.51
$ToMOH_{peroxo}$	n/a	n/a	0.54	0.67
ToMOH $T201S_{peroxo}$	675	1500	0.67	1.51

Table 7: Relevant Biochemical Data of ToMO Associated Proteins

Protein	Assembly	Length (amino acids)	Cofactors	Molecular Weight (kDa)	Extinction Coefficient (M^{-1} cm^{-1})	Uniprot ID	PDBID	Gene in *P.stutzeri* OX1
ToMOH	Dimer of trimers	α - 498 β - 330 γ - 86	2 Diiron Clusters	Complex ~212,00 α - 57,72 β - 38,334 γ - 9,973	A_{280} - 600,000	α- O87798 β- O87802 γ- O87799	1T0Q 2INC	α - touA β - touE γ - touB
ToMOH Apo	Dimer of trimers	α - 498 β - 330 γ - 86	None	Complex ~212,000 α - 57,72 β - 38,334 γ - 9,973	A_{280} - 525,000	N/A	N/A	α - touA β - touE γ - touB
ToMOD	Monomer	110	None	12,274	A_{280} -2980	Q6IV63	N/A	touD
ToMOC	Monomer	112	[2Fe-2S] cluster	12,504	A_{458} - 6870	Q6IV64	N/A	touC
ToMOF	Monomer	341	[2Fe-2S] cluster, C-terminal FAD-Domain	38,934	A_{454} - 48,100	Q6IV61	N/A	touF

Table 8: ToMO / T4MO Residues Demonstrating Significant Differential Mobility in sMMOH versus ToMOH

Residue Number in ToMO	Fold Change in Mobility in sMMO vs. T4MO
185	55
37	29.9
188	23.7
119	21.2
180	15.6
106	15.6
186	14.5
187	14.2
44	13.4
28	13.1
100	11.8
155	10.7
127	10
249	8.9
191	8.7
250	8.3
245	8
414	7.9
193	7.6
43	7.5
175	7.4
104	7.4
128	7.4
319	7.1
246	7